

HHO methods for the incompressible Navier-Stokes and the incompressible Euler equations

Lorenzo Botti · Francesco Carlo Massa[†]

Received: date / Accepted: date

Abstract We propose two Hybrid High-Order (HHO) methods for the incompressible Navier-Stokes equations and investigate their robustness with respect to the Reynolds number. While both methods rely on a HHO formulation of the viscous term, the pressure-velocity coupling is fundamentally different, up to the point that the two approaches can be considered antithetical. The first method is kinetic energy preserving, meaning that the skew-symmetric discretization of the convective term is guaranteed not to alter the kinetic energy balance. The approximated velocity fields exactly satisfy the divergence free constraint and continuity of the normal component of the velocity is weakly enforced on the mesh skeleton, leading to H-div conformity. The second scheme relies on Godunov fluxes for pressure-velocity coupling: a Harten, Lax and van Leer (HLL) approximated Riemann Solver designed for cell centered formulations is adapted to hybrid face centered formulations. The resulting numerical scheme is robust up to the inviscid limit, meaning that it can be applied for seeking approximate solutions of the incompressible Euler equations. The schemes are numerically validated performing steady and unsteady two dimensional test cases and evaluating the convergence rates on h -refined mesh sequences. In addition to standard benchmark flow problems, specifically conceived test cases are conducted for studying the error behaviour when approaching the inviscid limit.

Keywords Hybrid High-Order · Navier–Stokes equations · Euler equations · Pressure-robust · Pointwise divergence free

Mathematics Subject Classification (2020) MSC 65M60 · MSC 76B47 · MSC 76D05

1 Introduction

In this work we propose and numerically validate two Hybrid High-Order (HHO) methods for the Incompressible Navier-Stokes (INS) equations, governing the flow of incompressible fluids. For the sake of simplicity, we focus on a Newtonian fluid with uniform density. Given a polygonal or polyhedral domain $\Omega \subset \mathbb{R}^d$, $d \in \{2, 3\}$, with boundary $\partial\Omega$,

Lorenzo Botti
Università degli Studi di Bergamo
Dipartimento di Ingegneria e Scienze Applicate
Tel.: +39 035 2052150
Fax.: +39 035 2052310
E-mail: lorenzo.botti@unibg.it

[†] *corresponding author*

Francesco Carlo Massa
Università degli Studi di Bergamo
Dipartimento di Ingegneria e Scienze Applicate
Tel.: +39 035 2052002
E-mail: francescocarlo.massa@unibg.it

the initial velocity field $\mathbf{u}_0 : \Omega \rightarrow \mathbb{R}^d$ and a finite time t_F the incompressible Navier-Stokes problem consists in finding the velocity field $\mathbf{u} : \Omega \times (0, t_F) \rightarrow \mathbb{R}^d$, and the pressure field $p : \Omega \times (0, t_F) \rightarrow \mathbb{R}$, such that

$$\frac{\partial \mathbf{u}}{\partial t} + \nabla \cdot [(\mathbf{u} \otimes \mathbf{u}) + p\mathbf{I} - \nu \nabla \mathbf{u}] = \mathbf{f} \quad \text{in } \Omega \times (0, t_F), \quad (1a)$$

$$\nabla \cdot \mathbf{u} = 0 \quad \text{in } \Omega \times (0, t_F), \quad (1b)$$

$$\mathbf{u} = \mathbf{g}_D \quad \text{on } \partial\Omega_D \times (0, t_F). \quad (1c)$$

$$\mathbf{n} \cdot [p\mathbf{I} - \nu \nabla \mathbf{u}] = \mathbf{g}_N \quad \text{on } \partial\Omega_N \times (0, t_F), \quad (1d)$$

where \mathbf{n} denotes the unit vector normal to $\partial\Omega$ pointing out of Ω , ν is the (constant) viscosity, \mathbf{g}_D and \mathbf{g}_N denote, respectively, the prescribed velocity on the Dirichlet boundary $\partial\Omega_D \subset \partial\Omega$ and the prescribed traction on the Neumann boundary $\partial\Omega_N := \partial\Omega \setminus \partial\Omega_D$, while $\mathbf{f} : \Omega \rightarrow \mathbb{R}^d$ is a given body force. It is assumed in what follows that both $\partial\Omega_D$ and $\partial\Omega_N$ have non-zero $(d-1)$ -dimensional Hausdorff measure (otherwise, additional closure conditions are needed).

HHO methods are gaining momentum in the field of continuum mechanics having been successfully applied to nonlinear elasticity problems [1, 19], diffusion dominated incompressible flow problems [2, 38], porous-media flows [18] and poro-elasticity problems [15, 16]. Similarly to Hybridizable Discontinuous Galerkin (HDG) methods, HHO formulations rely on Degrees Of Freedom (DOFs) associated to polynomial functions defined over mesh elements and mesh faces, the so called elemental and skeletal DOFs. Since solely skeletal DOFs are globally coupled, in particular the face based stencil consist of all mesh faces belonging to the boundary of the two elements sharing the face, elemental degrees of freedom can be eliminated by computing the Schur complement. This procedure is known as *static condensation*. Thanks to static condensations, HHO Jacobian matrices are sparse block matrices whose block size is driven by the dimension of polynomial spaces in $d-1$ variables when considering a d -dimensional flow problem. Accordingly, when accuracy is improved by means of higher-degree p -type expansions, the number of Jacobian matrix non-zero entries grows slower than Discontinuous Galerkin (DG) methods, thereby reducing the computational cost associated to matrix-vector products as well as matrices memory footprint. From the matrix assembly viewpoint HHO methods are generally more expensive than DG methods, also due to the computational cost of static condensation, nevertheless matrix assembly and static condensation are intrinsically parallel tasks that are expected to show optimal scalability on multicore and manycore architectures. Besides computational efficiency considerations, HHO formulations have demonstrated to be robust with respect to mesh distortion and grading [5, 17]. These features are of crucial importance in the context of CFD applications, where boundary layers are commonly employed to improve the resolution near wall.

Since the pioneering works [27, 29–32] dating back to the late 1980s, DG methods have gained increased popularity in computational fluid mechanics, boosted by the 1997 landmark papers [8, 9] on the viscous terms treatment. In the context of incompressible flow problems, stabilized pressure-velocity was proposed by Cockburn *et al.* [28] while Bassi *et al.* [11] exploited the artificial compressibility idea of Chorin [25] to define suitable Godunov fluxes. Shahbazi *et al.* [57] proposed a semi-explicit time integration with nonlinear terms handled by means of local Lax–Friedrichs fluxes. The extension of DG methods to general polyhedral meshes was theoretically conceived in [35] and [36], leading to adaptive mesh coarsening by agglomeration [6] and high-order accurate geometry representation with arbitrarily coarse meshes [7, 10]. *hp*-Versions and handling of meshes with small faces have been considered in [3, 4]; see also the recent monograph [22]. More recently, Tavelli and Dumbser [58, 59] and Dumbser *et al.* [41] proposed to use staggered meshes, while Manzanero *et al.* [52] devised an entropy-stable nodal dG spectral element method.

Since the seminal work of Nguyen *et al.* [54], later analyzed by Cesmelioglu *et al.* [24], several HDG discretizations of the incompressible Navier-Stokes equations have been proposed. We mention in particular the *energy stable* and momentum conserving formulation devised by Labeur *et al.* [50] and the superconvergent method by Qiu *et al.* [55]. More recently, Rhebergen *et al.* [56] devised a pointwise divergence free formulation, later analysed by Kirk *et al.* [48]. HHO discretizations of the Navier-Stokes equations have been originally considered in [39, 40]. A kinetic energy preserving formulation was proposed by Botti *et al.* [14], see also [34, Chapters 8 and 9] for further details. Robustness with respect to large irrotational body forces was considered by Castanon *et al.* [23] while extension to non-Newtonian fluids was considered by Botti *et al.* [20].

In this work, we consider two HHO schemes that are novel variations of existing schemes with improved features. In both cases, the Dirichlet condition on the velocity is enforced weakly in the spirit of [14]. The first scheme borrows

the skew-symmetric convective term treatment proposed by Botti *et al.* [14], while the pressure-velocity coupling is inspired by the Hybridizable Discontinuous Galerkin (HDG) method of [56]. Likewise the latter HDG formulation, the method is kinetic energy preserving and yields an exactly divergence free H-div conforming velocity approximation. Pressure-robustness is also guaranteed, meaning that the pressure error does not influence the velocity error. We use polynomials of degree $k + 1$ and k to approximate the velocity and the pressure over mesh elements, respectively. Polynomials of degree $k + 1$, $k + 1$ and k are employed to approximate the numerical trace of the pressure on mesh faces, velocity on Neumann boundary faces and velocity on internal and Dirichlet boundary faces, respectively. With respect to the HDG formulation of [56], thanks to HHO treatment of the viscous terms in the spirit of [26] (see also [34, Section 5.1]), improved orders of convergence are gained on simplicial meshes: in particular we observe $k + 2$ and $k + 1$ convergence rate for the velocity and pressure error in L^2 norm, respectively. Note that the leading block size of the statically condensed Jacobian matrix is driven by skeletal velocity DOFs, mostly associated to polynomials functions of degree k . The second scheme targets robustness in the inviscid limit. Indeed, as we shall demonstrate by means of numerical test cases, the formulation is able to cope with the incompressible Euler equations. Inspired by DG methods based on Godunov fluxes, see *e.g.*, [11, 12, 42, 53] and following the ideas proposed by [61] we employ an Harten, Lax and van Leer (HLL) approximated Riemann solver for designing pressure-velocity coupling and convective term treatment. The scheme relies on polynomials of degree k for both elemental and skeletal unknowns resulting in convergence rates of order $k + 1$ for both the velocity and pressure error in L^2 norm. Moreover, in the diffusion dominated regime, order $k + 2$ for the velocity is recovered.

The paper is organized as follows. After introducing the discrete settings and the HHO discretization of the viscous term that the two formulations share in common, see Sections 2.1-2.2, the HHO-Hdiv and HHO-HLL formulations of the incompressible Navier-Stokes equations are provided in Sections 2.4 and 2.5, respectively. Notable features of the proposed formulations are outlined in Section 2.4.2, which focus on H-div conformity of HHO-Hdiv, and Section 2.5.2, which outlines the derivation of the HLL-type Riemann solver which HHO-HLL is based upon. In Section 3 we tackle several flow configurations, namely Kovaszny flow (Section 3.1), LLMS pressure gradient (Section 3.2), Gresho-Chan vortex (Section 3.3), double shear layer (3.4), and lid-driven cavity flow (Section 3.5).

2 Two HHO methods for the Navier-Stokes problem

2.1 Discrete setting

The HHO formulations proposed in this work allow to deal with two and three dimensional flow problems. Nevertheless, since numerical test cases focus on two space dimensions, discrete settings are provided for the 2D case. We consider meshes of the domain Ω corresponding to couples $\mathcal{M}_h := (\mathcal{T}_h, \mathcal{F}_h)$, where \mathcal{T}_h is a finite collection of polygonal elements such that $h := \max_{T \in \mathcal{T}_h} h_T > 0$ with h_T denoting the diameter of T , while \mathcal{F}_h is a finite collection of line segments. Extension to 3D requires to consider meshes composed of polyhedral elements and polygonal faces. It is assumed henceforth that the mesh \mathcal{M}_h is shape and contact regular, as detailed in [34, Definition 1.4]. For each mesh element $T \in \mathcal{T}_h$, the faces contained in the element boundary ∂T are collected in the set \mathcal{F}_T , and, for each mesh face $F \in \mathcal{F}_h$, \mathcal{T}_F is the set containing the one or two mesh elements sharing F . We define three disjoint subsets of the set \mathcal{F}_T : the set of Dirichlet boundary faces $\mathcal{F}_T^D := \{F \in \mathcal{F}_T : F \subset \partial\Omega_D\}$; the set of Neumann boundary faces $\mathcal{F}_T^N := \{F \in \mathcal{F}_T : F \subset \partial\Omega_N\}$; the set of internal faces $\mathcal{F}_T^i := \mathcal{F}_T \setminus (\mathcal{F}_T^D \cup \mathcal{F}_T^N)$. For future use, we also let $\mathcal{F}_T^{i,D} := \mathcal{F}_T^i \cup \mathcal{F}_T^D$. Using the same arguments we define three disjoint subsets of the set \mathcal{F}_h : \mathcal{F}_h^D , \mathcal{F}_h^N , \mathcal{F}_h^i and we let $\mathcal{F}_h^{i,D} := \mathcal{F}_h^i \cup \mathcal{F}_h^D$. For all $T \in \mathcal{T}_h$ and all $F \in \mathcal{F}_T$, \mathbf{n}_{TF} denotes the unit vector normal to F pointing out of T .

Hybrid High-Order methods hinge on local polynomial spaces on mesh elements and faces. For given integers $\ell \geq 0$ and $n \geq 1$, we denote by \mathbb{P}_n^ℓ the space of n -variate polynomials of total degree $\leq \ell$ (in short, of degree ℓ). For X mesh element or face, we denote by $\mathcal{P}^\ell(X)$ the space spanned by the restriction to X of functions in \mathbb{P}_d^ℓ . When X is a mesh face, the resulting space is isomorphic to \mathbb{P}_{d-1}^ℓ (see [34, Proposition 1.23]).

Let again X denote a mesh element or face. The local L^2 -orthogonal projector $\pi_X^\ell : L^2(X) \rightarrow \mathcal{P}^\ell(X)$ is such that, for all $q \in L^2(X)$,

$$\int_X (q - \pi_X^\ell q) r = 0 \quad \forall r \in \mathcal{P}^\ell(X).$$

Notice that, above and in what follows, we omit the measure from integrals as it can always be inferred from the context. The L^2 -orthogonal projector on $\mathcal{P}^\ell(X)^d$, obtained applying π_X^ℓ component-wise, is denoted by π_X^ℓ .

2.2 HHO discretization of the Laplace operator

The HHO discretizations of the Navier-Stokes problem considered in this work hinge on velocity reconstructions devised at the element level and obtained assembling diffusive potential reconstructions component-wise. In what follows, we let a mesh element $T \in \mathcal{T}_h$ be fixed, denote by $k \geq 0$ the degree of polynomials attached to internal and Dirichlet mesh faces, by $t \in \{k, k+1\}$ the degree of polynomials attached to mesh elements and by $f \in \{k, k+1\}$ the degree of polynomials attached to Neumann faces. We remark that, the motivation for choosing t and f one degree higher than k will be given in Section 2.4.2.

2.2.1 Scalar potential reconstruction

The velocity reconstruction is obtained leveraging, for each component, the *scalar potential reconstruction* originally introduced in [37] in the context of scalar diffusion problems (see also [26] and [34, Section 5.1] for its generalization to the case of different polynomial degrees on elements and faces). Define the local scalar HHO space

$$\underline{V}_T^{t,k,f} := \left\{ \underline{v}_T = (v_T, (v_F)_{F \in \mathcal{F}_T}) : v_T \in \mathcal{P}^t(T), v_F \in \mathcal{P}^k(F) \text{ for all } F \in \mathcal{F}_T^{i,D} \text{ and } v_F \in \mathcal{P}^f(F) \text{ for all } F \in \mathcal{F}_T^N \right\}. \quad (2)$$

The scalar potential reconstruction operator $\mathfrak{p}_T^{k+1} : \underline{V}_T^{t,k,f} \rightarrow \mathcal{P}^{k+1}(T)$ maps a vector of polynomials of $\underline{V}_T^{t,k,f}$ onto a polynomial of degree $(k+1)$ over T as follows: Given $\underline{v}_T \in \underline{V}_T^{t,k,f}$, $\mathfrak{p}_T^{k+1} \underline{v}_T$ is the unique polynomial in $\mathcal{P}^{k+1}(T)$ satisfying

$$\begin{aligned} \int_T \nabla \mathfrak{p}_T^{k+1} \underline{v}_T \cdot \nabla w_T &= \int_T \nabla v_T \cdot \nabla w_T + \sum_{F \in \mathcal{F}_T} \int_F (v_F - v_T) \nabla w_T \cdot \mathbf{n}_{TF} \quad \forall w_T \in \mathcal{P}^{k+1}(T), \\ \int_T \mathfrak{p}_T^{k+1} \underline{v}_T &= \int_T v_T. \end{aligned}$$

Computing \mathfrak{p}_T^{k+1} for each $T \in \mathcal{T}_h$ requires to solve a small linear system. This task shows optimal scalability on parallel architectures.

2.2.2 Velocity reconstruction

Define, in analogy with (2), the following vector-valued HHO space for the velocity:

$$\underline{V}_T^{t,k,f} := \left\{ \underline{v}_T = (v_T, (v_F)_{F \in \mathcal{F}_T}) : v_T \in \mathcal{P}^t(T)^d, v_F \in \mathcal{P}^k(F)^d \text{ for all } F \in \mathcal{F}_T^{i,D} \text{ and } v_F \in \mathcal{P}^f(F)^d \text{ for all } F \in \mathcal{F}_T^N \right\}. \quad (3)$$

The *velocity reconstruction* $\mathfrak{B}_T^{k+1} : \underline{V}_T^{t,k,f} \rightarrow \mathcal{P}^{k+1}(T)^d$ is obtained setting

$$\mathfrak{B}_T^{k+1} \underline{v}_T := (\mathfrak{p}_T^{k+1} v_{T,i})_{i=1,\dots,d},$$

where, for all $i = 1, \dots, d$, $v_{T,i} \in \underline{V}_T^{t,k,f}$ is obtained gathering the i th components of the polynomials in \underline{v}_T , i.e., $v_{T,i} := (v_{T,i}, (v_{F,i})_{F \in \mathcal{F}_T})$ if $v_T = (v_{T,i})_{i=1,\dots,d}$ and $v_F = (v_{F,i})_{i=1,\dots,d}$ for all $F \in \mathcal{F}_T$.

The local interpolation operator $\underline{\mathbf{I}}_T^{t,k,f} : H^1(T)^d \rightarrow \underline{\mathbf{V}}_T^{t,k,f}$ is defined as follows: For all $\mathbf{v} \in H^1(T)^d$,

$$\underline{\mathbf{I}}_T^{t,k,f} \mathbf{v} := (\pi_T^t \mathbf{v}, (\pi_F^k \mathbf{v}|_F)_{F \in \mathcal{F}_T^{i,D}}, (\pi_F^f \mathbf{v}|_F)_{F \in \mathcal{F}_T^N}). \quad (4)$$

Following [34, Section 5.1.3], it is possible to demonstrate that the velocity reconstruction is such that, for all $\mathbf{v} \in H^1(T)^d$

$$\int_T (\nabla \mathfrak{P}_T^{k+1} \underline{\mathbf{I}}_T^{t,k,f} \mathbf{v} - \nabla \mathbf{v}) : \nabla \mathbf{w}_T = 0 \text{ for all } \mathbf{w}_T \in \mathcal{P}^{k+1}(T)^d \text{ and } \int_T \mathfrak{P}_T^{k+1} \underline{\mathbf{I}}_T^{t,k,f} \mathbf{v} = \int_T \mathbf{v}. \quad (5)$$

The above result is of crucial importance for inferring the approximation properties of the velocity reconstruction operator.

2.2.3 Face residuals

Let $T \in \mathcal{T}_h$ and $F \in \mathcal{F}_T$. The stabilization bilinear form for the HHO discretization of the viscous term in the momentum equation (1a) hinges on the residual operator $\mathbf{r}_{TF}^k : \underline{\mathbf{V}}_T^{t,k,f} \rightarrow \underline{\mathbf{V}}_T^{t,k,f}$ defined as follows

$$\mathbf{r}_{TF}^k \underline{\mathbf{v}}_T := \mathbf{r}_F^{k,f} \underline{\mathbf{v}}_T - \mathbf{r}_F^t \underline{\mathbf{v}}_T$$

where the *face residual* $\mathbf{r}_F^{k,f} : \underline{\mathbf{V}}_T^{t,k,f} \rightarrow \mathcal{P}^{k,f}(F)$ and the *element residual* $\mathbf{r}_F^t : \underline{\mathbf{V}}_T^{t,k,f} \rightarrow \mathcal{P}^t(T)$ such that, for all $\underline{\mathbf{v}}_T \in \underline{\mathbf{V}}_T^{t,k,f}$,

$$\mathbf{r}_F^{k,f} \underline{\mathbf{v}}_T := \begin{cases} \pi_F^k (v_F - \mathfrak{p}_T^{k+1} \underline{\mathbf{v}}_T) & \text{if } F \in \mathcal{F}_h^{i,D} \\ \pi_F^f (v_F - \mathfrak{p}_T^{k+1} \underline{\mathbf{v}}_T) & \text{if } F \in \mathcal{F}_h^N \end{cases} \quad \text{and} \quad \mathbf{r}_F^t \underline{\mathbf{v}}_T := \pi_T^t (v_T - \mathfrak{p}_T^{k+1} \underline{\mathbf{v}}_T).$$

The vector residual $\mathfrak{R}_{TF}^k : \underline{\mathbf{V}}_T^{t,k,f} \rightarrow \underline{\mathbf{V}}_T^{t,k,f}$ is such that, for all $\underline{\mathbf{v}}_T \in \underline{\mathbf{V}}_T^{t,k,f}$:

$$\mathfrak{R}_{TF}^k \underline{\mathbf{v}}_T := (\mathbf{r}_{TF}^k \underline{\mathbf{v}}_T, i)_{i=1, \dots, d}.$$

2.3 Local and global HHO spaces for velocity and pressure unknowns

In addition to the scalar and vector valued local velocity spaces $\underline{\mathbf{V}}_T^{t,k,f}$ and $\underline{\mathbf{V}}_T^{t,k,f}$ defined in (2) and (3), respectively, we need to introduce local pressure spaces and global HHO spaces for both velocity and pressure.

Let $T \in \mathcal{T}_h$ and define the local scalar HHO space for the pressure unknown

$$\underline{\mathcal{Q}}_T^{k,p} := \left\{ q_T = (q_T, (q_F)_{F \in \mathcal{F}_T}) : q_T \in \mathcal{P}^k(T) \text{ and } q_F \in \mathcal{P}^p(F) \text{ for all } F \in \mathcal{F}_T \right\}, \quad (6)$$

where $p \in \{k, k+1\}$. The global scalar HHO space is defined and follows

$$\underline{\mathcal{Q}}_h^{k,p} := \left\{ q_h = ((q_T)_{T \in \mathcal{T}_h}, (q_F)_{F \in \mathcal{F}_h}) : q_T \in \mathcal{P}^k(T) \text{ for all } T \in \mathcal{T}_h \text{ and } q_F \in \mathcal{P}^p(F) \text{ for all } F \in \mathcal{F}_h \right\}.$$

For all $q_h \in \underline{\mathcal{Q}}_h^{k,p}$ and all $T \in \mathcal{T}_h$, we denote by $q_T \in \underline{\mathcal{Q}}_T^{k,p}$ the restriction of q_h to T .

To conclude, the global vector HHO space reads

$$\underline{\mathbf{V}}_h^{t,k,f} := \left\{ \underline{\mathbf{v}}_h = ((v_T)_{T \in \mathcal{T}_h}, (v_F)_{F \in \mathcal{F}_h}) : \begin{cases} v_T \in \mathcal{P}^t(T)^d \text{ for all } T \in \mathcal{T}_h, \\ v_F \in \mathcal{P}^k(F)^d \text{ for all } F \in \mathcal{F}_h^{i,D}, \\ v_F \in \mathcal{P}^f(F)^d \text{ for all } F \in \mathcal{F}_h^N \end{cases} \right\}.$$

For all $\underline{\mathbf{v}}_h \in \underline{\mathbf{V}}_h^{t,k,f}$ and all $T \in \mathcal{T}_h$, we denote by $\underline{\mathbf{v}}_T \in \underline{\mathbf{V}}_T^{t,k,f}$ the restriction of $\underline{\mathbf{v}}_h$ to T .

2.4 A pointwise divergence free H-div conforming HHO scheme

2.4.1 Local and global residuals

We combine the HHO discretization of the viscous term with a hybrid approximation of the pressure inspired by [56]. Given $(\underline{\mathbf{u}}_T, \underline{p}_T) \in \mathbf{V}_T^{t,k,f} \times \underline{Q}_T^{k,p}$, the local residuals $r_{I,T}^{\text{mnt}}((\underline{\mathbf{u}}_T, \underline{p}_T); \cdot) : \mathbf{V}_T^{t,k,f} \rightarrow \mathbb{R}$ of the space discrete momentum and $r_{I,T}^{\text{cnt}}(\underline{\mathbf{u}}_T; \cdot) : \underline{Q}_T^{k,p} \rightarrow \mathbb{R}$ of the discrete mass conservation equations are such that, for all $\underline{\mathbf{v}}_T \in \mathbf{V}_T^{t,k,f}$ and all $\underline{q}_T \in \underline{Q}_T^{k,p}$,

$$\begin{aligned}
r_{I,T}^{\text{mnt}}((\underline{\mathbf{u}}_T, \underline{p}_T); \underline{\mathbf{v}}_T) &:= \int_T \nu \nabla \mathfrak{B}_T^{k+1} \underline{\mathbf{u}}_T : \nabla \mathfrak{B}_T^{k+1} \underline{\mathbf{v}}_T + \sum_{F \in \mathcal{F}_T} \frac{\nu}{h_F} \int_F \mathfrak{R}_{TF}^k \underline{\mathbf{v}}_T \cdot \mathfrak{R}_{TF}^k \underline{\mathbf{v}}_T \\
&\quad - \sum_{F \in \mathcal{F}_T^{\text{D}}} \int_F [(\mathbf{n}_{TF} \cdot \nu \nabla \mathfrak{B}_T^{k+1} \underline{\mathbf{u}}_T) \cdot \mathbf{v}_F + \mathbf{u}_F \cdot (\mathbf{n}_{TF} \cdot \nu \nabla \mathfrak{B}_T^{k+1} \underline{\mathbf{v}}_T)] + \sum_{F \in \mathcal{F}_T^{\text{D}}} \frac{\eta \nu}{h_F} \int_F \mathbf{u}_F \cdot \mathbf{v}_F \\
&\quad - \int_T p_T (\nabla \cdot \mathbf{v}_T) + \sum_{F \in \mathcal{F}_T} \int_F p_F (\mathbf{v}_T - \mathbf{v}_F) \cdot \mathbf{n}_{TF} + \sum_{F \in \mathcal{F}_T^{\text{D}}} \int_F p_F (\mathbf{v}_F \cdot \mathbf{n}_{TF}) \\
&\quad + \frac{1}{2} \left(\int_T (\mathbf{u}_T \cdot \nabla \mathbf{u}_T) \cdot \mathbf{v}_T - \int_T (\mathbf{u}_T \otimes \mathbf{u}_T) : \nabla \mathbf{v}_T + \sum_{F \in \mathcal{F}_T} \int_F (\mathbf{u}_F \cdot \mathbf{n}_{TF}) (\mathbf{u}_F \cdot \mathbf{v}_T - \mathbf{u}_T \cdot \mathbf{v}_F) \right) \\
&\quad + \frac{1}{2} \left(\sum_{F \in \mathcal{F}_T^{\text{D}}} \int_F (\mathbf{u}_F \cdot \mathbf{n}_{TF}) \mathbf{g}_D \cdot \mathbf{v}_F + \sum_{F \in \mathcal{F}_T^{\text{N}}} \int_F (\mathbf{u}_F \cdot \mathbf{n}_{TF}) \mathbf{u}_T \cdot \mathbf{v}_F \right) \\
&\quad - \sum_{F \in \mathcal{F}_T^{\text{D}}} \int_F \mathbf{g}_D \cdot \left(\mathbf{n}_{TF} \cdot \nu \nabla \mathfrak{B}_T^{k+1} \underline{\mathbf{v}}_T + \frac{\eta \nu}{h_F} \mathbf{v}_F \right) - \sum_{F \in \mathcal{F}_T^{\text{N}}} \int_F \mathbf{g}_N \cdot \mathbf{v}_F + \int_T \left(\frac{\partial \mathbf{u}_T}{\partial t} - \mathbf{f} \right) \cdot \mathbf{v}_T, \\
r_{I,T}^{\text{cnt}}(\underline{\mathbf{u}}_T; \underline{q}_T) &:= - \int_T (\nabla \cdot \mathbf{u}_T) q_T + \sum_{F \in \mathcal{F}_T} \int_F (\mathbf{u}_T - \mathbf{u}_F) \cdot \mathbf{n}_{TF} q_F + \sum_{F \in \mathcal{F}_T^{\text{D}}} \int_F (\mathbf{u}_F - \mathbf{g}_D) \cdot \mathbf{n}_{TF} q_F
\end{aligned}$$

In the expression of $r_{I,T}^{\text{mnt}}((\underline{\mathbf{u}}_T, \underline{p}_T); \cdot)$, $\eta > 0$ is a user-dependent parameter that has to be taken large enough to ensure coercivity. The penalty term where the parameter η appears, along with the consistency terms in the second line and the terms involving the boundary datum \mathbf{g}_D in the fifth and sixth lines, are responsible for the weak enforcement of Dirichlet boundary conditions for the velocity. In the numerical tests provided below, η is taken equal to 3.

The global residuals $r_{I,h}^{\text{mnt}}((\underline{\mathbf{u}}_h, \underline{p}_h); \cdot) : \mathbf{V}_h^{t,k,f} \rightarrow \mathbb{R}$ and $r_{I,h}^{\text{cnt}}(\underline{\mathbf{u}}_h; \cdot) : \underline{Q}_h^{k,p} \rightarrow \mathbb{R}$ are obtained by element-by-element assembly of the local residuals, *i.e.*: For all $\underline{\mathbf{v}}_h \in \mathbf{V}_h^{t,k,f}$ and all $\underline{q}_h \in \underline{Q}_h^{k,p}$,

$$r_{I,h}^{\text{mnt}}((\underline{\mathbf{u}}_h, \underline{p}_h); \underline{\mathbf{v}}_h) := \sum_{T \in \mathcal{T}_h} r_{I,T}^{\text{mnt}}((\underline{\mathbf{u}}_T, \underline{p}_T); \underline{\mathbf{v}}_T), \quad r_{I,h}^{\text{cnt}}(\underline{\mathbf{u}}_h; \underline{q}_h) := \sum_{T \in \mathcal{T}_h} r_{I,T}^{\text{cnt}}(\underline{\mathbf{u}}_T; \underline{q}_T). \quad (8)$$

The HHO scheme with pointwise divergence free H-div conforming velocity field is obtained setting the polynomial degrees as $t = f = p = k + 1$.

Scheme I (HHO-Hdiv) Find $(\underline{\mathbf{u}}_h, \underline{p}_h) \in \mathbf{V}_h^{k+1,k,k+1} \times \underline{Q}_h^{k,k+1}$ such that

$$\begin{aligned}
r_{I,h}^{\text{mnt}}((\underline{\mathbf{u}}_h, \underline{p}_h); \underline{\mathbf{v}}_h) &= 0 & \forall \underline{\mathbf{v}}_h \in \mathbf{V}_h^{k+1,k,k+1}, \\
r_{I,h}^{\text{cnt}}(\underline{\mathbf{u}}_h; \underline{q}_h) &= 0 & \forall \underline{q}_h \in \underline{Q}_h^{k,k+1}.
\end{aligned} \quad (9)$$

2.4.2 Discrete mass conservation and H-div conformity

For each $\underline{\mathbf{u}}_h \in \underline{\mathbf{V}}_h^{t,k,f}$, $r_{T,h}^{\text{cnt}} = 0$ for all $\underline{\mathbf{q}}_h \in \underline{\mathbf{Q}}_h^{k,p}$ implies that

1. if $q_F = 0$ for all $F \in \mathcal{F}_h$, then $\int_T (\nabla \cdot \mathbf{u}_T) q_T = 0$, for each $T \in \mathcal{T}_h$;
2. if $q_T = 0$ for all $T \in \mathcal{T}_h$, then $\begin{cases} \int_F (\mathbf{u}_T - \mathbf{u}_{T'}) \cdot \mathbf{n}_{TF} q_F = 0, & \text{for each } F \in \mathcal{F}_T^i \cap \mathcal{F}_{T'}^i, \text{ with } T, T' \in \mathcal{T}_h, T \neq T'; \\ \int_F (\mathbf{u}_T - \mathbf{u}_F) \cdot \mathbf{n}_{TF} q_F = 0, & \text{for each } T \in \mathcal{T}_h, F \in \mathcal{F}_T^N; \\ \int_F (\mathbf{u}_T - \mathbf{g}_D) \cdot \mathbf{n}_{TF} q_F = 0, & \text{for each } T \in \mathcal{T}_h, F \in \mathcal{F}_T^D. \end{cases}$

Setting $t = f = p = k + 1$, it is straightforward to conclude that

$$\nabla \cdot \mathbf{u}_T = 0, \quad \forall \mathbf{x} \in T, \quad \forall T \in \mathcal{T}_h; \quad (10)$$

$$(\mathbf{u}_T - \mathbf{u}_{T'}) \cdot \mathbf{n}_{TF} = 0, \quad \forall \mathbf{x} \in F, \quad \text{for each } F \in \mathcal{F}_T^i \cap \mathcal{F}_{T'}^i, \text{ with } T, T' \in \mathcal{T}_h, T \neq T'; \quad (11)$$

$$(\mathbf{u}_T - \mathbf{u}_F) \cdot \mathbf{n}_{TF} = 0, \quad \forall \mathbf{x} \in F, \quad \text{for each } T \in \mathcal{T}_h, F \in \mathcal{F}_T^N; \quad (12)$$

$$(\mathbf{u}_T - \pi_F^{k+1} \mathbf{g}_D) \cdot \mathbf{n}_{TF} = 0, \quad \forall \mathbf{x} \in F, \quad \text{for each } T \in \mathcal{T}_h, F \in \mathcal{F}_T^D. \quad (13)$$

Remark 1 (Polynomial degree of velocity unknowns over Neumann faces) When $t = p = k + 1$, choosing $f = k + 1$ is mandatory to ensure H-div conformity on Neumann faces without constraining velocity unknowns over mesh elements. Note in particular that setting $f = k$ would imply that, according to (12), $\mathbf{u}_T|_F \in \mathcal{P}^k(F)$ for each $F \in \mathcal{F}_h^N$. We also remark that setting $f = k$ is perfectly fine if \mathbf{g}_N is a constant, in particular traction-free boundary conditions commonly employed on outflow sections of channel flows can be dealt with without raising the polynomial degree on outflow faces.

Remark 2 (h-Convergence rates on simplicial and general meshes) The HHO-Hdiv formulations show convergence rates of order $k + 1$ for the pressure error in L^2 norm on both simplicial and general meshes. Convergence rates of order $k + 2$ and $k + 1$ for the velocity and velocity gradients error in L^2 norm, respectively, are attained on simplicial meshes, while, on general meshes, convergence rates are reduced by one order. Choosing $t = k + 1$ and $f = p = k$ allows to recover optimal convergence rates for the velocity on general meshes but H-div conformity and pressure-robustness are lost. Indeed, (11)-(12)-(13) are replaced by the following looser conditions on the normal trace of the velocity

$$(\pi_F^k \mathbf{u}_T - \pi_F^k \mathbf{u}_{T'}) \cdot \mathbf{n}_{TF} = 0, \quad \forall \mathbf{x} \in F, \quad \text{for each } F \in \mathcal{F}_T^i \cap \mathcal{F}_{T'}^i, \text{ with } T, T' \in \mathcal{T}_h, T \neq T'; \quad (14)$$

$$(\pi_F^k \mathbf{u}_T - \mathbf{u}_F) \cdot \mathbf{n}_{TF} = 0, \quad \forall \mathbf{x} \in F, \quad \text{for each } T \in \mathcal{T}_h, F \in \mathcal{F}_T^N \quad (15)$$

$$(\pi_F^k \mathbf{u}_T - \pi_F^k \mathbf{g}_D) \cdot \mathbf{n}_{TF} = 0, \quad \forall \mathbf{x} \in F, \quad \text{for each } T \in \mathcal{T}_h, F \in \mathcal{F}_T^D \quad (16)$$

Since (10) holds, the method yields a pointwise divergence free velocity field. The HHO scheme with pointwise divergence free velocity and optimal convergence properties on general meshes is outlined in what follows for the sake of completeness.

Scheme II (HHO-DivFree) Find $(\underline{\mathbf{u}}_h, \underline{\mathbf{p}}_h) \in \underline{\mathbf{V}}_h^{k+1,k,k} \times \underline{\mathbf{Q}}_h^{k,k}$ such that

$$\begin{aligned} r_{T,h}^{\text{mnt}}((\underline{\mathbf{u}}_h, \underline{\mathbf{p}}_h); \underline{\mathbf{v}}_h) &= 0 & \forall \underline{\mathbf{v}}_h \in \underline{\mathbf{V}}_h^{k+1,k,k+1}, \\ r_{T,h}^{\text{cnt}}(\underline{\mathbf{u}}_h; \underline{\mathbf{q}}_h) &= 0 & \forall \underline{\mathbf{q}}_h \in \underline{\mathbf{Q}}_h^{k,k+1}. \end{aligned} \quad (17)$$

2.5 A HHO formulation robust in the inviscid limit

2.5.1 Local and global residuals

Given $(\underline{\mathbf{u}}_T, \underline{\mathbf{p}}_T) \in \underline{\mathbf{V}}_T^{t,k,f} \times \underline{\mathbf{Q}}_T^{k,p}$, the local residuals $r_{II,T}^{\text{mnt}}((\underline{\mathbf{u}}_T, \underline{\mathbf{p}}_T); \cdot) : \underline{\mathbf{V}}_T^{t,k,f} \rightarrow \mathbb{R}$ of the space discrete momentum and $r_{II,T}^{\text{cnt}}(\underline{\mathbf{u}}_T; \cdot) : \underline{\mathbf{Q}}_T^{k,p} \rightarrow \mathbb{R}$ of the discrete mass conservation equations are such that, for all $\underline{\mathbf{v}}_T \in \underline{\mathbf{V}}_T^{t,k,f}$ and all $\underline{\mathbf{q}}_T \in \underline{\mathbf{Q}}_T^{k,p}$,

$$\begin{aligned}
r_{II,T}^{\text{mnt}}((\underline{\mathbf{u}}_T, \underline{\mathbf{p}}_T); \underline{\mathbf{v}}_T) &:= \int_T \nu \nabla \mathfrak{P}_T^{k+1} \underline{\mathbf{u}}_T : \nabla \mathfrak{P}_T^{k+1} \underline{\mathbf{v}}_T + \sum_{F \in \mathcal{F}_T} \frac{\nu}{h_F} \int_F \mathfrak{R}_{TF}^k \underline{\mathbf{v}}_T \cdot \mathfrak{R}_{TF}^k \underline{\mathbf{v}}_T \\
&\quad - \sum_{F \in \mathcal{F}_T^{\text{D}}} \int_F [(\mathbf{n}_{TF} \cdot \nu \nabla \mathfrak{P}_T^{k+1} \underline{\mathbf{u}}_T) \cdot \mathbf{v}_F + \mathbf{u}_F \cdot (\mathbf{n}_{TF} \cdot \nu \nabla \mathfrak{P}_T^{k+1} \underline{\mathbf{v}}_T)] + \sum_{F \in \mathcal{F}_T^{\text{D}}} \frac{\eta \nu}{h_F} \int_F \mathbf{u}_F \cdot \mathbf{v}_F \\
&\quad - \sum_{F \in \mathcal{F}_T^{\text{D}}} \int_F \mathbf{g}_D \cdot \left(\mathbf{n}_{TF} \cdot \nu \nabla \mathfrak{P}_T^{k+1} \underline{\mathbf{v}}_T + \frac{\eta \nu}{h_F} \mathbf{v}_F \right) - \int_T p_T (\nabla \cdot \mathbf{v}_T) + \sum_{F \in \mathcal{F}_T} \int_F p_F (\mathbf{v}_T \cdot \mathbf{n}_{TF}) \\
&\quad - \int_T (\mathbf{u}_T \otimes \mathbf{u}_T) : \nabla \mathbf{v}_T + \sum_{F \in \mathcal{F}_T} \int_F (\mathbf{u}_F \cdot \mathbf{n}_{TF}) \mathbf{u}_F \cdot \mathbf{v}_T + \sum_{F \in \mathcal{F}_T} \int_F s^+(\mathbf{u}_T - \mathbf{u}_F) \cdot (\mathbf{v}_T - \mathbf{v}_F) \\
&\quad + \sum_{F \in \mathcal{F}_T^{\text{D}}} \int_F s^-(\mathbf{g}_D - \mathbf{u}_F) \cdot \mathbf{v}_F - \sum_{F \in \mathcal{F}_T^{\text{N}}} \int_F (\mathbf{g}_N - p_F \mathbf{n}_{TF}) \cdot \mathbf{v}_F + \int_T \left(\frac{\partial \mathbf{u}_T}{\partial t} - \mathbf{f} \right) \cdot \mathbf{v}_T, \\
r_{II,T}^{\text{cnt}}(\underline{\mathbf{u}}_T; \underline{\mathbf{q}}_T) &:= - \int_T \mathbf{u}_T \cdot \nabla q_T + \sum_{F \in \mathcal{F}_T} \int_F \mathbf{u}_F \cdot \mathbf{n}_{TF} q_T + \sum_{F \in \mathcal{F}_T} \int_F \frac{s^+}{a^2} (p_T - p_F) (q_T - q_F) \\
&\quad + \sum_{F \in \mathcal{F}_T^{\text{N}}} \int_F \frac{s^-}{a^2} \left((\mathbf{g}_N + \mathbf{n}_{TF} \cdot \nu \nabla \mathfrak{P}_T^{k+1} \underline{\mathbf{u}}_T) \cdot \mathbf{n}_{TF} - p_F \right) q_F,
\end{aligned}$$

where

$$s^\pm = \frac{1}{2} \left(\mathbf{u}_F \cdot \mathbf{n}_{TF} \pm \sqrt{(\mathbf{u}_F \cdot \mathbf{n}_{TF})^2 + 4a^2} \right) \quad (19)$$

and a is the artificial compressibility parameter. In the numerical tests provided below, a is taken as a unit velocity. In the expression of $r_{II,T}^{\text{mnt}}((\underline{\mathbf{u}}_T, \underline{\mathbf{p}}_T); \cdot)$, $\eta > 0$ is a user-dependent parameter that has to be taken large enough to ensure coercivity. In the numerical tests provided below, η is taken equal to 3.

The global residuals $r_{II,h}^{\text{mnt}}((\underline{\mathbf{u}}_h, \underline{\mathbf{p}}_h); \cdot) : \underline{\mathbf{V}}_h^{t,k,f} \rightarrow \mathbb{R}$ and $r_{II,h}^{\text{cnt}}(\underline{\mathbf{u}}_h; \cdot) : \underline{\mathbf{Q}}_h^{k,p} \rightarrow \mathbb{R}$ are obtained by element-by-element assembly of the local residuals, *i.e.*: For all $\underline{\mathbf{v}}_h \in \underline{\mathbf{V}}_h^{t,k,f}$ and all $\underline{\mathbf{q}}_h \in \underline{\mathbf{Q}}_h^{k,p}$,

$$r_{II,h}^{\text{mnt}}((\underline{\mathbf{u}}_h, \underline{\mathbf{p}}_h); \underline{\mathbf{v}}_h) := \sum_{T \in \mathcal{T}_h} r_{II,T}^{\text{mnt}}((\underline{\mathbf{u}}_T, \underline{\mathbf{p}}_T); \underline{\mathbf{v}}_T), \quad r_{II,h}^{\text{cnt}}(\underline{\mathbf{u}}_h; \underline{\mathbf{q}}_h) := \sum_{T \in \mathcal{T}_h} r_{II,T}^{\text{cnt}}(\underline{\mathbf{u}}_T; \underline{\mathbf{q}}_T). \quad (20)$$

The HHO scheme based on the HLL Riemann solver is obtained setting the polynomial degrees as $t = f = p = k$.

Scheme III (HHO-HLL) Find $(\underline{\mathbf{u}}_h, \underline{\mathbf{p}}_h) \in \underline{\mathbf{V}}_h^{k,k,k} \times \underline{\mathbf{Q}}_h^{k,k}$ such that

$$\begin{aligned}
r_{II,h}^{\text{mnt}}((\underline{\mathbf{u}}_h, \underline{\mathbf{p}}_h); \underline{\mathbf{v}}_h) &= 0 & \forall \underline{\mathbf{v}}_h \in \underline{\mathbf{V}}_h^{k,k,k}, \\
r_{II,h}^{\text{cnt}}(\underline{\mathbf{u}}_h; \underline{\mathbf{q}}_h) &= 0 & \forall \underline{\mathbf{q}}_h \in \underline{\mathbf{Q}}_h^{k,k}.
\end{aligned} \quad (21)$$

2.5.2 Artificial compressibility based HLL-type numerical flux

In order to outline the convective term and pressure-velocity coupling formulations we focus on the inviscid framework and, for the sake of conciseness, we assume that periodic boundary conditions are imposed over $\partial\Omega$. Accordingly, the local residuals for the HHO-HLL discretization of the Euler equations on a periodic domain reads: given $(\underline{\mathbf{u}}_T, \underline{p}_T) \in \mathbf{V}_T^{k,k,k} \times \underline{Q}_T^{k,k}$, for all $\underline{\mathbf{v}}_T \in \mathbf{V}_T^{k,k,k}$ and all $\underline{q}_T \in \underline{Q}_T^{k,k}$

$$r_{II,T}^{\text{mnt}}((\underline{\mathbf{u}}_T, \underline{p}_T); \underline{\mathbf{v}}_T) = \int_T (\mathbf{u}_T \otimes \mathbf{u}_T + p_T \mathbf{I}) : \nabla \mathbf{v}_T + \int_T \left(\frac{\partial \mathbf{u}_T}{\partial t} - \mathbf{f} \right) \cdot \mathbf{v}_T + \sum_{F \in \mathcal{F}_T} \int_F [(\mathbf{u}_F \otimes \mathbf{u}_F + p_F \mathbf{I}) \cdot \mathbf{n}_{TF} + s^+(\mathbf{u}_T - \mathbf{u}_F)] \cdot (\mathbf{v}_T - \mathbf{v}_F), \quad (22)$$

$$r_{II,T}^{\text{cnt}}(\underline{\mathbf{u}}_T; \underline{q}_T) = - \int_T \mathbf{u}_T \cdot \nabla q_T + \sum_{F \in \mathcal{F}_T} \int_F \left[\mathbf{u}_F \cdot \mathbf{n}_{TF} + \frac{s^+}{a^2} (p_T - p_F) \right] (q_T - q_F). \quad (23)$$

The terms within square brackets are the, so called, *numerical fluxes* of the HHO formulation.

In order to outline the trace conditions enforced over mesh faces we now consider the global residuals of the Euler equations with Dirichlet and Neumann boundary conditions imposed over $\partial\Omega$. For each $(\underline{\mathbf{u}}_h, \underline{p}_h) \in \mathbf{V}_h^{k,k,k} \times \underline{Q}_h^{k,k}$, $r_{II,h}^{\text{mnt}} = 0$ for all $\underline{\mathbf{v}}_h \in \mathbf{V}_h^{k,k,k}$ such that $\mathbf{v}_T = 0$ for all $T \in \mathcal{T}_h$, implies that

$$\begin{aligned} \int_F [s^+(\mathbf{u}_T - \mathbf{u}_F) - s^-(\mathbf{u}_{T'} - \mathbf{u}_F)] \cdot \mathbf{v}_F &= 0, & \text{for each } F \in \mathcal{F}_T^i \cap \mathcal{F}_{T'}^i, \text{ with } T, T' \in \mathcal{T}_h, T \neq T'; \\ \int_F s^+(\mathbf{u}_T - \mathbf{u}_F) \cdot \mathbf{v}_F &= 0, & \text{for each } T \in \mathcal{T}_h, F \in \mathcal{F}_T^{\text{N}}; \\ \int_F [s^+(\mathbf{u}_T - \mathbf{u}_F) - s^-(\mathbf{g}_D - \mathbf{u}_F)] \cdot \mathbf{v}_F &= 0, & \text{for each } T \in \mathcal{T}_h, F \in \mathcal{F}_T^{\text{D}}. \end{aligned}$$

For each $\underline{\mathbf{u}}_h \in \mathbf{V}_h^{k,k,k}$, $r_{II,h}^{\text{cnt}} = 0$ for all $\underline{q}_h \in \underline{Q}_h^{k,k}$ such that $q_T = 0$ for all $T \in \mathcal{T}_h$, implies that

$$\begin{aligned} \int_F [s^+(p_T - p_F) - s^-(p_{T'} - p_F)] q_F &= 0, & \text{for each } F \in \mathcal{F}_T^i \cap \mathcal{F}_{T'}^i, \text{ with } T, T' \in \mathcal{T}_h, T \neq T'; \\ \int_F [s^+(p_T - p_F) - s^-(\mathbf{g}_N \cdot \mathbf{n}_{TF} - p_F)] q_F &= 0, & \text{for each } T \in \mathcal{T}_h, F \in \mathcal{F}_T^{\text{N}}; \\ \int_F s^+(p_T - p_F) q_F &= 0, & \text{for each } T \in \mathcal{T}_h, F \in \mathcal{F}_T^{\text{D}}. \end{aligned}$$

Accordingly, the intermediate state at each $F \in \mathcal{F}_T^i \cap \mathcal{F}_{T'}^i$, is the weighted average between the two neighbour element (T, T') states, *i.e.*,

$$\boldsymbol{\pi}_F^k((s^+ - s^-)\mathbf{u}_F) = \boldsymbol{\pi}_F^k(s^+\mathbf{u}_T - s^-\mathbf{u}_{T'}) \quad \text{and} \quad \boldsymbol{\pi}_F^k((s^+ - s^-)p_F) = \boldsymbol{\pi}_F^k(s^+p_T - s^-p_{T'}). \quad (24)$$

The HHO-HLL formulation falls into the generalized framework of Riemann solvers for hybrid DG methods proposed by Vila-Pérez *et al.* [61] and is based on the Exact Riemann Solver (ERS) for variable density incompressible flows devised in [12]. In particular, following [60], the ERS based HLL Riemann solver can be derived: the flux $_{\star}$ in the *star* region delimited by the two external acoustic waves reads

$$\begin{aligned} (\mathbf{u} \otimes \mathbf{u} + p\mathbf{I})_{\star} \cdot \mathbf{n}_{FT} &= \frac{s_{T'}(\mathbf{u}_T \otimes \mathbf{u}_T + p_T \mathbf{I}) - s_T(\mathbf{u}_{T'} \otimes \mathbf{u}_{T'} + p_{T'} \mathbf{I})}{s_{T'} - s_T} \cdot \mathbf{n}_{FT} + \frac{s_{T'} s_T}{s_{T'} - s_T} (\mathbf{u}_{T'} - \mathbf{u}_T), \\ (\mathbf{u})_{\star} \cdot \mathbf{n}_{FT} &= \frac{s_T \mathbf{u}_T - s_T \mathbf{u}_{T'}}{s_{T'} - s_T} \cdot \mathbf{n}_{FT} + \frac{s_{T'} s_T}{s_{T'} - s_T} \frac{1}{a^2} (p_{T'} - p_T). \end{aligned}$$

The two external acoustic wave speeds are

$$s_{T'} = \frac{1}{2} \left(\mathbf{u}_{T'} \cdot \mathbf{n}_{TF} + \sqrt{(\mathbf{u}_{T'} \cdot \mathbf{n}_{TF})^2 + 4a^2} \right) \quad \text{and} \quad s_T = \frac{1}{2} \left(\mathbf{u}_T \cdot \mathbf{n}_{TF} - \sqrt{(\mathbf{u}_T \cdot \mathbf{n}_{TF})^2 + 4a^2} \right),$$

regardless of the compressive or expansive nature of the acoustic waves, see Appendix B4 in [12] for details. Defining the intermediate state as

$$\mathbf{u}_F = \frac{s_{T'} \mathbf{u}_T - s_T \mathbf{u}_{T'}}{s_{T'} - s_T} \quad \text{and} \quad p_F = \frac{s_{T'} p_T - s_T p_{T'}}{s_{T'} - s_T},$$

and performing some trivial algebraic manipulations, the flux_★ can be written as follows

$$\begin{aligned} (\mathbf{u} \otimes \mathbf{u} + p \mathbf{I})_{\star} \cdot \mathbf{n}_{FT} &= (\mathbf{u}_F \otimes \mathbf{u}_T + p_F \mathbf{I}) \cdot \mathbf{n}_{FT} + s_{T'} (\mathbf{u}_T - \mathbf{u}_F) - \frac{s_T}{s_{T'} - s_T} \mathbf{u}_{T'} [(\mathbf{u}_{T'} - \mathbf{u}_T) \cdot \mathbf{n}_{TF}], \\ (\mathbf{u})_{\star} \cdot \mathbf{n}_{FT} &= \mathbf{u}_F \cdot \mathbf{n}_{FT} + s_{T'} \frac{1}{a^2} (p_T - p_F). \end{aligned}$$

In order to decouple neighboring elements, the continuity of the normal component of the velocity is assumed by hypothesis, namely $\mathbf{u}_T \cdot \mathbf{n}_{TF} = \mathbf{u}_{T'} \cdot \mathbf{n}_{TF} = \mathbf{u}_F \cdot \mathbf{n}_{TF}$. Thus, the numerical fluxes in Equations (22)–(23) as well as the interface conditions in (24) and the wave speeds in (19) are directly obtained. We remark that, according to the HLL machinery, see [60] for details, unique definition of numerical fluxes follows from the observation that $s_{T'} > 0$ and $s_T < 0$.

3 Numerical results

3.1 Kovasznay flow

Steady flow behind a grid made of equally spaced parallel rods is described by the following exact solution of the incompressible Navier–Stokes equations (see [49])

$$\begin{aligned} \mathbf{u} &= [1 - e^{\kappa x} \cos(2\pi y)] \mathbf{i} + \frac{\kappa}{2\pi} e^{\kappa x} \sin(2\pi y) \mathbf{j}, \\ p &= p_0 - \frac{1}{2} e^{2\kappa x}, \end{aligned} \tag{25}$$

where $p_0 \in \mathbb{R}$ is an arbitrary constant and the parameter κ depends on the Reynolds number

$$\kappa = \frac{\text{Re}}{2} - \sqrt{\frac{\text{Re}^2}{4} + 4\pi^2}.$$

The Kovasznay flow problem is defined on the bi-unit square computational domain $\Omega = (-0.5, 1.5) \times (0, 2)$ and solved by means of the HHO–Hdiv and HHO–HLL schemes. Boundary conditions are derived from the Kovasznay analytical solution (25) at $\text{Re} = \frac{1}{\nu} = 40$. In particular, a Neumann boundary condition is imposed at the outflow boundary (right side of the square domain) while Dirichlet boundary conditions are imposed on the remaining boundaries.

In order to numerically validate the proposed HHO schemes, we consider h -refined mesh sequences composed of regular triangular and quadrilateral elements, doubling the number of mesh elements in each Cartesian direction at each refinement step, and several polynomial degrees $k = \{1, 2, 3, 4\}$. Errors in L^2 -norm and h -convergence rates are tabulated for the approximated pressure, divergence of the velocity, velocity, and velocity gradients fields. Results over triangular elements meshes are reported in Tables 1 and 2 for HHO–Hdiv and HHO–HLL schemes, respectively. Results over quadrilateral elements meshes are reported in Tables 3 and 4 for HHO–Hdiv and HHO–HLL schemes, respectively. As a general observation it can be noticed that, although the level of accuracy provided by the two schemes proposed is comparable, the HHO–Hdiv scheme takes the lead over triangular elements meshes while HHO–HLL is to be preferred over quadrilateral meshes.

Table 1 Kovaszny flow. Errors and h -convergence rates for the HHO-Hdiv scheme on the triangular elements mesh sequence.

	card(\mathcal{T}_h)	$\ \nabla \mathbf{u}_T - \nabla \mathbf{u}\ _{L^2}$	order	$\ \mathbf{u}_T - \mathbf{u}\ _{L^2}$	order	$\ p_T - p\ _{L^2}$	order	$\ \nabla \cdot \mathbf{u}_T\ _{L^2}$	order
$k = 1$	32	2.42e+00	–	1.08e-01	–	5.68e-02	–	7.32e-16	–
	128	8.90e-01	1.44	2.58e-02	2.07	1.82e-02	1.64	5.74e-16	–
	512	2.99e-01	1.57	3.63e-03	2.83	4.99e-03	1.87	4.74e-16	–
	2048	8.51e-02	1.81	4.96e-04	2.87	1.18e-03	2.08	5.19e-16	–
	8192	2.28e-02	1.90	6.65e-05	2.90	2.87e-04	2.03	5.09e-16	–
$k = 2$	32	9.24e-01	–	3.78e-02	–	1.52e-02	–	6.60e-16	–
	128	1.60e-01	2.52	3.05e-03	3.63	1.46e-03	3.38	6.91e-16	–
	512	2.33e-02	2.78	1.72e-04	4.15	1.97e-04	2.89	5.52e-16	–
	2048	3.80e-03	2.61	1.46e-05	3.55	2.73e-05	2.85	5.68e-16	–
	8192	4.75e-04	3.00	8.96e-07	4.03	3.08e-06	3.15	5.48e-16	–
$k = 3$	32	1.95e-01	–	4.85e-03	–	2.13e-03	–	6.73e-16	–
	128	2.10e-02	3.21	2.69e-04	4.17	1.75e-04	3.60	6.88e-16	–
	512	1.83e-03	3.52	1.02e-05	4.73	1.23e-05	3.84	5.45e-16	–
	2048	1.24e-04	3.89	3.43e-07	4.89	6.67e-07	4.20	5.99e-16	–
	8192	8.14e-06	3.92	1.12e-08	4.93	4.04e-08	4.04	5.99e-16	–
$k = 4$	32	4.44e-02	–	9.20e-04	–	3.63e-04	–	7.73e-16	–
	128	2.02e-03	4.46	2.51e-05	5.19	1.10e-05	5.04	7.01e-16	–
	512	7.67e-05	4.72	3.19e-07	6.30	3.65e-07	4.92	6.03e-16	–
	2048	3.32e-06	4.53	7.31e-09	5.45	1.35e-08	4.76	6.33e-16	–
	8192	9.90e-08	5.07	1.05e-10	6.12	3.84e-10	5.13	6.30e-16	–

Since the flow is diffusion dominated at this Reynolds number, the HHO-HLL scheme shows an asymptotic convergence rates of $k + 2$ for the velocity and $k + 1$ for pressure, velocity divergence and velocity gradients. The convergence rates obtained over quadrilateral elements meshes are slightly better than those on triangular elements meshes, at all polynomial degrees. Notice that, at the same mesh sequence refinement step, quadrilateral meshes have twice the number of elements as compared to triangular meshes.

HHO-Hdiv scheme shows asymptotic convergence rates of order $k + 1$ for the pressure unknown on both triangular and quadrilateral meshes. The incompressibility constraint is exactly satisfied, note that the velocity divergence errors settle around the machine precision. Convergence rates for the velocity and the velocity gradients differs when applying HHO-Hdiv on triangular and quadrilateral elements meshes. On triangular meshes we observe the optimal rates of $k + 2$ and $k + 1$ for the velocity and the velocity gradients, respectively, while on quadrilateral meshes the convergence tops at $k + 1$ and k , respectively. Accordingly, a full order of convergence is lost. We refer to the work of Kirk *et al.* [48] for additional clues regarding improved convergence rates on simplices.

Eventually, as remarked in Section 2.4.2, we verify that optimal convergence rates on quadrilateral meshes can be recovered by lowering the degree of polynomials employed to approximate the numerical trace of the pressure on mesh faces. Results for the HHO-DivFree scheme on the quadrilateral mesh sequence are reported in Table 5. Since the HHO-DivFree scheme is not H-div conforming and has demonstrated to be less robust than HHO-HLL in convection-dominated flow regimes, it will not be further investigated in subsequent test cases.

3.2 LLMS pressure gradient test case

In order to investigate pressure-robustness, *i.e.*, velocity solution accuracy in the presence of strong pressure gradients [51, 56], we consider the test case proposed by Lederer, Linke, Merdon and Schöberl (LLMS) [51], hereinafter referred to as LLMS pressure gradient test case. We impose boundary conditions and forcing term \mathbf{f} according to the following analytical velocity and pressure fields

$$\mathbf{u} = \nabla \times \zeta \quad \text{and} \quad p = p_0 + x^7 + y^7,$$

with arbitrary $p_0 \in \mathbb{R}$ and $\zeta = x^2(x-1)^2 y^2(y-1)^2$. In case of HHO-Hdiv we impose Dirichlet boundary conditions on all but one side of the unit square domain $\Omega = (0, 1) \times (0, 1)$, where a Neumann boundary is set. In order to ensure stability in the inviscid limit, in case of HHO-HLL we impose both Dirichlet and Neumann boundary conditions on all sides, leading to the so called *given* boundary conditions. We remark that, according to given BCs, HLL Riemann

Table 2 Kovaszny flow. Errors and h -convergence rates for the HHO-HLL scheme on the triangular element mesh sequence.

	$\text{card}(\mathcal{T}_h)$	$\ \nabla \mathbf{u}_T - \nabla \mathbf{u}\ _{L^2}$	order	$\ \mathbf{u}_T - \mathbf{u}\ _{L^2}$	order	$\ p_T - p\ _{L^2}$	order	$\ \nabla \cdot \mathbf{u}_T\ _{L^2}$	order
$k = 1$	32	3.22e+00	–	3.30e-01	–	2.38e-01	–	4.80e-01	–
	128	1.46e+00	1.22	7.54e-02	2.28	4.70e-02	2.50	3.62e-01	0.41
	512	5.23e-01	1.45	1.30e-02	2.49	7.56e-03	2.59	1.42e-01	1.35
	2048	1.66e-01	1.71	1.89e-03	2.88	1.38e-03	2.55	5.36e-02	1.41
	8192	4.76e-02	1.79	2.66e-04	2.81	2.65e-04	2.36	1.75e-02	1.61
$k = 2$	32	1.37e+00	–	8.12e-02	–	6.24e-02	–	2.65e-01	–
	128	2.10e-01	2.89	7.22e-03	3.73	4.67e-03	3.99	4.87e-02	2.44
	512	3.20e-02	2.67	4.95e-04	3.80	3.83e-04	3.54	8.45e-03	2.53
	2048	5.29e-03	2.69	4.32e-05	3.64	5.34e-05	2.95	1.47e-03	2.52
	8192	7.22e-04	2.85	2.97e-06	3.84	6.94e-06	2.92	2.21e-04	2.73
$k = 3$	32	2.22e-01	–	1.06e-02	–	3.99e-03	–	3.97e-02	–
	128	2.23e-02	3.54	5.15e-04	4.65	2.70e-04	4.15	4.93e-03	3.01
	512	1.96e-03	3.45	2.41e-05	4.34	1.95e-05	3.72	4.63e-04	3.41
	2048	1.44e-04	3.90	8.77e-07	4.95	1.41e-06	3.93	4.01e-05	3.53
	8192	9.91e-06	3.84	3.08e-08	4.80	9.03e-08	3.94	2.95e-06	3.76
$k = 4$	32	4.44e-02	–	1.63e-03	–	1.10e-03	–	1.14e-02	–
	128	1.78e-03	4.95	3.24e-05	6.04	2.27e-05	5.98	4.42e-04	4.69
	512	6.99e-05	4.59	6.46e-07	5.54	8.01e-07	4.74	1.93e-05	4.52
	2048	3.02e-06	4.70	1.47e-08	5.66	3.12e-08	4.85	8.39e-07	4.52
	8192	1.05e-07	4.81	2.62e-10	5.77	1.09e-09	4.82	3.07e-08	4.77

Table 3 Kovaszny flow. Errors and h -convergence rates for the HHO-Hdiv scheme on the quadrilateral elements mesh sequence.

	$\text{card}(\mathcal{T}_h)$	$\ \nabla \mathbf{u}_T - \nabla \mathbf{u}\ _{L^2}$	order	$\ \mathbf{u}_T - \mathbf{u}\ _{L^2}$	order	$\ p_T - p\ _{L^2}$	order	$\ \nabla \cdot \mathbf{u}_T\ _{L^2}$	order
$k = 1$	64	4.01e+00	–	1.40e-01	–	2.93e-02	–	3.91e-16	–
	256	1.99e+00	1.01	3.53e-02	1.99	7.96e-03	1.88	3.14e-16	–
	1024	9.90e-01	1.00	8.97e-03	1.98	2.27e-03	1.81	3.18e-16	–
	4096	4.94e-01	1.00	2.26e-03	1.99	5.98e-04	1.93	2.79e-16	–
	16384	2.47e-01	1.00	5.67e-04	1.99	1.52e-04	1.97	3.04e-16	–
$k = 2$	64	8.88e-01	–	1.96e-02	–	4.01e-03	–	3.12e-16	–
	256	2.15e-01	2.05	2.33e-03	3.07	3.31e-04	3.60	3.67e-16	–
	1024	5.32e-02	2.01	2.84e-04	3.04	2.36e-05	3.81	3.42e-16	–
	4096	1.33e-02	2.00	3.52e-05	3.01	1.78e-06	3.73	3.34e-16	–
	16384	3.31e-03	2.00	4.39e-06	3.00	1.59e-07	3.49	3.75e-16	–
$k = 3$	64	1.26e-01	–	1.82e-03	–	2.67e-04	–	3.32e-16	–
	256	1.53e-02	3.04	1.15e-04	3.98	2.29e-05	3.54	3.63e-16	–
	1024	1.90e-03	3.01	7.22e-06	3.99	1.57e-06	3.87	3.60e-16	–
	4096	2.36e-04	3.00	4.52e-07	4.00	1.00e-07	3.97	3.39e-16	–
	16384	2.95e-05	3.00	2.83e-08	4.00	6.31e-09	3.99	3.70e-16	–
$k = 4$	64	1.35e-02	–	1.46e-04	–	2.12e-05	–	3.29e-16	–
	256	8.16e-04	4.05	4.32e-06	5.08	4.33e-07	5.61	3.67e-16	–
	1024	5.04e-05	4.02	1.32e-07	5.03	8.65e-09	5.64	4.06e-16	–
	4096	3.14e-06	4.00	4.11e-09	5.01	2.00e-10	5.44	3.94e-16	–
	16384	1.96e-07	4.00	1.28e-10	5.00	5.40e-12	5.21	4.30e-16	–

problems on boundary faces utilize both the analytical pressure and velocity solutions for the definition of external states.

Figure 1 shows the horizontal velocity component ($\mathbf{u} \cdot \mathbf{i}$) and pressure behavior over the computational domain. Notice the presence of a strong pressure gradient near the top-right corner of the square.

In order to numerically validate convergence rates in the diffusion dominated and convection dominated flow regimes we consider $\nu = 1$ and $\nu = 10^{-4}$, respectively. The computational domain is discretized by means of increasingly fine regular triangular elements meshes, doubling the number of elements in each Cartesian direction at each refinement step, and we focus on $k = 3$ HHO formulations. Tables 6-9 summarize the convergence analysis considering errors in L^2 -norm for the velocity, the velocity gradients and the pressure fields. In the diffusion dominated regime both HHO-Hdiv and HHO-HLL deliver the same convergence rates, *i.e.*, order $k + 2$ for the velocity and $k + 1$ for pressure

Table 4 Kovaszny flow. Errors and h -convergence rates for the HHO-HLL scheme on the quadrilateral elements mesh sequence.

	$\text{card}(\mathcal{T}_h)$	$\ \nabla \mathbf{u}_T - \nabla \mathbf{u}\ _{L^2}$	order	$\ \mathbf{u}_T - \mathbf{u}\ _{L^2}$	order	$\ p_T - p\ _{L^2}$	order	$\ \nabla \cdot \mathbf{u}_T\ _{L^2}$	order
$k = 1$	64	2.11e+00	–	1.08e-01	–	7.82e-02	–	1.38e-01	–
	256	7.63e-01	1.53	1.67e-02	2.82	1.20e-02	2.82	8.86e-02	0.64
	1024	2.45e-01	1.67	2.69e-03	2.69	1.97e-03	2.67	3.44e-02	1.36
	4096	7.19e-02	1.79	4.12e-04	2.74	3.11e-04	2.69	1.07e-02	1.68
	16384	1.97e-02	1.88	5.82e-05	2.84	5.08e-05	2.63	2.99e-03	1.84
$k = 2$	64	3.42e-01	–	1.39e-02	–	6.62e-03	–	3.70e-02	–
	256	5.94e-02	2.64	1.28e-03	3.59	7.09e-04	3.36	7.78e-03	2.25
	1024	9.17e-03	2.75	9.73e-05	3.80	5.73e-05	3.71	1.39e-03	2.48
	4096	1.29e-03	2.86	6.77e-06	3.89	5.61e-06	3.39	2.13e-04	2.71
	16384	1.73e-04	2.92	4.48e-07	3.94	6.49e-07	3.13	2.97e-05	2.84
$k = 3$	64	4.17e-02	–	1.23e-03	–	5.86e-04	–	7.60e-03	–
	256	3.25e-03	3.84	5.05e-05	4.80	2.54e-05	4.72	7.69e-04	3.30
	1024	2.35e-04	3.87	1.92e-06	4.82	1.28e-06	4.41	6.43e-05	3.58
	4096	1.61e-05	3.91	6.73e-08	4.89	5.72e-08	4.53	4.85e-06	3.73
	16384	1.06e-06	3.94	2.24e-09	4.94	2.66e-09	4.45	3.38e-07	3.84
$k = 4$	64	3.73e-03	–	8.16e-05	–	4.07e-05	–	5.57e-04	–
	256	1.49e-04	4.84	1.59e-06	5.93	1.12e-06	5.41	2.01e-05	4.79
	1024	5.38e-06	4.90	2.80e-08	5.95	3.29e-08	5.20	7.31e-07	4.78
	4096	1.81e-07	4.94	4.67e-10	5.97	9.85e-10	5.12	2.57e-08	4.83
	16384	5.91e-09	4.97	7.57e-12	5.98	2.97e-11	5.08	8.95e-10	4.84

Table 5 Kovaszny flow. Errors and h -convergence rates for the HHO-DivFree scheme on the quadrilateral elements mesh sequence.

	$\text{card}(\mathcal{T}_h)$	$\ \nabla \mathbf{u}_T - \nabla \mathbf{u}\ _{L^2}$	order	$\ \mathbf{u}_T - \mathbf{u}\ _{L^2}$	order	$\ p_T - p\ _{L^2}$	order	$\ \nabla \cdot \mathbf{u}_T\ _{L^2}$	order
$k = 1$	64	1.26e+00	–	5.65e-02	–	2.11e-02	–	1.73e-16	–
	256	3.07e-01	2.04	6.25e-03	3.18	2.33e-03	3.18	2.23e-16	–
	1024	7.63e-02	2.01	7.80e-04	3.00	5.17e-04	2.17	2.92e-16	–
	4096	1.91e-02	2.00	9.83e-05	2.99	1.28e-04	2.02	3.31e-16	–
	16384	4.79e-03	2.00	1.24e-05	2.99	3.19e-05	2.00	3.17e-16	–
$k = 2$	64	2.63e-01	–	6.64e-03	–	2.03e-03	–	2.02e-16	–
	256	3.46e-02	2.93	4.53e-04	3.87	1.78e-04	3.51	2.72e-16	–
	1024	4.42e-03	2.97	2.91e-05	3.96	1.42e-05	3.65	2.95e-16	–
	4096	5.58e-04	2.98	1.84e-06	3.98	1.26e-06	3.49	3.69e-16	–
	16384	7.02e-05	2.99	1.16e-07	3.99	1.32e-07	3.26	3.44e-16	–
$k = 3$	64	3.93e-02	–	6.28e-04	–	1.58e-04	–	1.97e-16	–
	256	2.64e-03	3.90	2.07e-05	4.93	4.46e-06	5.15	2.92e-16	–
	1024	1.70e-04	3.96	6.67e-07	4.95	1.79e-07	4.64	3.40e-16	–
	4096	1.08e-05	3.98	2.11e-08	4.98	7.91e-09	4.50	3.86e-16	–
	16384	6.77e-07	3.99	6.65e-10	4.99	3.64e-10	4.44	3.71e-16	–
$k = 4$	64	4.43e-03	–	5.07e-05	–	1.05e-05	–	2.39e-16	–
	256	1.49e-04	4.90	8.67e-07	5.87	2.61e-07	5.33	3.05e-16	–
	1024	4.76e-06	4.96	1.40e-08	5.96	6.45e-09	5.34	3.49e-16	–
	4096	1.50e-07	4.98	2.21e-10	5.98	1.76e-10	5.20	4.14e-16	–
	16384	4.73e-09	4.99	3.48e-12	5.99	5.13e-12	5.10	3.98e-16	–

Table 6 LLMS pressure gradient. Errors and h -convergence rates for $k = 3$ HHO-Hdiv with $\nu = 1$.

	$\text{card}(\mathcal{T}_h)$	$\ \nabla \mathbf{u}_T - \nabla \mathbf{u}\ _{L^2}$	order	$\ \mathbf{u}_T - \mathbf{u}\ _{L^2}$	order	$\ p_T - p\ _{L^2}$	order
	32	7.22e-04	–	1.02e-05	–	3.07e-04	–
	128	5.34e-05	3.76	4.05e-07	4.65	1.93e-05	3.99
	512	3.60e-06	3.89	1.43e-08	4.83	1.18e-06	4.04
	2048	2.34e-07	3.95	4.74e-10	4.91	7.20e-08	4.03
	8192	1.49e-08	3.97	1.53E-11	4.96	4.43e-09	4.02

and velocity gradients. In the convection dominated regime, only HHO-Hdiv maintains the aforementioned convergence rates, while the HHO-HLL scheme loses an order on velocity and velocity gradients fields.

Figure 2 depicts the pressure and velocity errors in L^2 -norm over the 2k triangular elements mesh for different viscosities values, *i.e.*, $\nu = \{1, 10^{-1}, 10^{-2}, 10^{-3}, 10^{-4}\}$. The fact that velocity errors are almost unaltered while varying

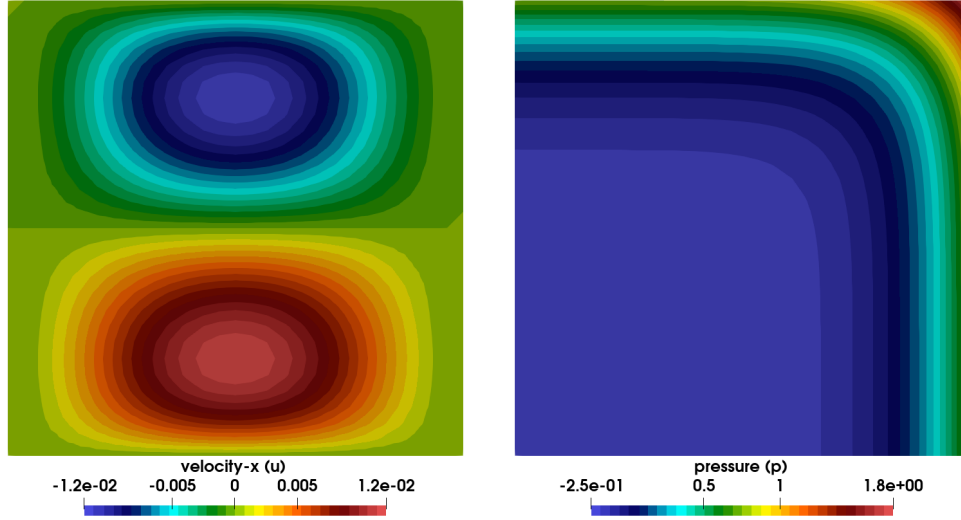


Fig. 1 LLMS pressure gradient. Horizontal velocity component (u) and pressure (p) fields ($p_0 = -0.25$).

Table 7 LLMS pressure gradient. Errors and h -convergence rates for $k = 3$ HHO-HLL with $\nu = 1$.

$\text{card}(\mathcal{T}_h)$	$\ \nabla \mathbf{u}_T - \nabla \mathbf{u}\ _{L^2}$	order	$\ \mathbf{u}_T - \mathbf{u}\ _{L^2}$	order	$\ p_T - p\ _{L^2}$	order
32	4.59e-04	–	1.14e-05	–	4.50e-04	–
128	2.85e-05	4.01	3.63e-07	4.97	2.94e-05	3.93
512	1.72e-06	4.05	1.14e-08	4.99	1.86e-06	3.99
2048	1.04e-07	4.04	3.59e-10	4.99	1.16e-07	4.00
8192	6.41e-09	4.03	1.13e-11	4.99	7.23e-09	4.00

Table 8 LLMS pressure gradient. Errors and h -convergence rates for $k = 3$ HHO-Hdiv with $\nu = 10^{-4}$.

$\text{card}(\mathcal{T}_h)$	$\ \nabla \mathbf{u}_T - \nabla \mathbf{u}\ _{L^2}$	order	$\ \mathbf{u}_T - \mathbf{u}\ _{L^2}$	order	$\ p_T - p\ _{L^2}$	order
32	1.59e-03	–	1.86e-05	–	2.58e-04	–
128	8.18e-05	4.28	5.51e-07	5.07	1.67e-05	3.95
512	6.62e-06	3.63	2.28e-08	4.60	1.05e-06	3.99
2048	4.72e-07	3.81	8.30e-10	4.78	6.60e-08	4.00
8192	3.09e-08	3.93	2.75e-11	4.92	4.13e-09	4.00

Table 9 LLMS pressure gradient. Errors and h -convergence rates for $k = 3$ HHO-HLL with $\nu = 10^{-4}$.

$\text{card}(\mathcal{T}_h)$	$\ \nabla \mathbf{u}_T - \nabla \mathbf{u}\ _{L^2}$	order	$\ \mathbf{u}_T - \mathbf{u}\ _{L^2}$	order	$\ p_T - p\ _{L^2}$	order
32	2.15e-02	–	5.77e-04	–	2.65e-04	–
128	2.22e-03	3.28	2.45e-05	4.56	1.72e-05	3.95
512	2.50e-04	3.15	1.24e-06	4.31	1.09e-06	3.98
2048	2.88e-05	3.12	6.85e-08	4.18	6.82e-08	3.99
8192	3.24e-06	3.15	3.88e-09	4.14	4.27e-09	4.00

the viscosity confirms that the HHO-Hdiv formulation is pressure-robust. Note that the velocity errors provided by the HHO-HLL scheme increase by two orders of magnitude while decreasing the viscosity by four orders of magnitude.

We next investigate robustness in the inviscid limit considering $k = 3$ and $k = 4$ HHO formulations over triangular and quadrilateral meshes and varying the viscosity in one order of magnitude steps from 1 to 10^{-14} . The error analysis reported in Figures 3 and 4 for different mesh densities, see figures captions for details, shows that pressure-robustness does not guarantee robustness in the inviscid limit. Indeed, only the HHO-HLL formulation is stable in the limit of vanishing viscosity. The velocity errors provided by the HHO-Hdiv formulation tend to dramatically increase for $\nu < 10^{-5}$. Moreover, due to convergence failure of Newton's method globalization strategy [47], the numerical solutions are not available for $\nu < 10^{-7}$. We verified that even using the L^2 -projection of the exact solution as initial guess the

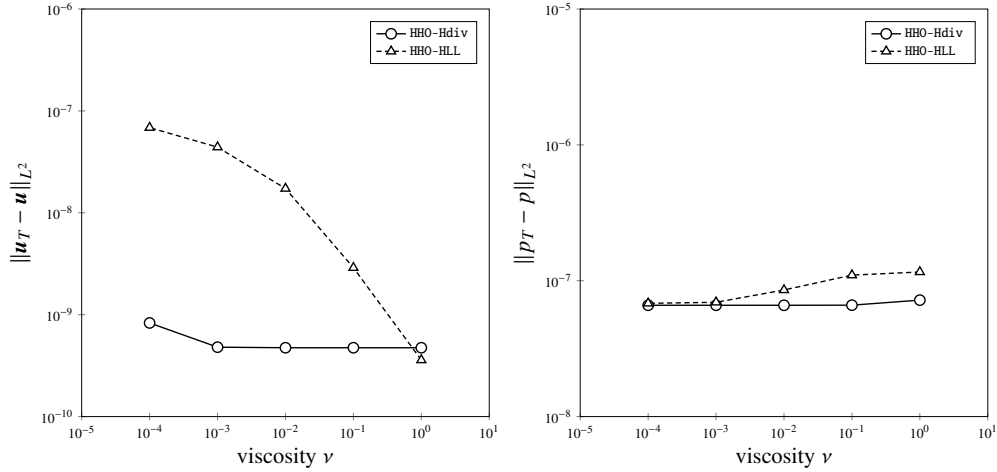


Fig. 2 LLMs pressure gradient. $k = 3$ HHO-Hdiv and HHO-HLL formulations on a 2048 triangular elements mesh. *Left and right*: Velocity and pressure errors in L^2 -norm, respectively, while changing the viscosity (ν).

simulation blows up. Interestingly, the HHO-HLL formulation shows to be resilient in the inviscid limit: notice that the velocity error reaches a plateau while decreasing the viscosity below 10^{-10} and also the pressure error is well behaved. In case of $k = 4$ HHO-HLL formulations over the 8k triangular and the 4k quadrilateral mesh, the velocity errors increase by three orders of magnitude moving from the diffusion dominated regime to the inviscid limit, while the pressure error stays almost constant around 10^{-11} .

3.3 Gresho-Chan vortex

Originally proposed by Gresho & Chan [46], who named it ‘triangular vortex’, this viscous 2D model problem is designed to study the schemes capability of preserving vortical structures. Our analysis relies on the numerical set-up described by Gauger *et al.* [44]: time integration is carried out over a double periodic unit squared domain $\Omega = (0, 1) \times (0, 1)$ based on the following initial conditions

$$(u, v, p) = (u_0, v_0, p_0) + \begin{cases} \left(-5\tilde{y}, 5\tilde{x}, \frac{25}{2}r^2 \right), & \text{if } 0 \leq r < 0.2, \\ \left(-2\frac{\tilde{y}}{r} + 5\tilde{y}, 2\frac{\tilde{x}}{r} - 5\tilde{x}, 4 \ln 5r + \frac{25}{2}r^2 - 20r + 4 \right), & \text{if } 0.2 \leq r < 0.4, \\ \left(0, 0, 4 \ln 2 - 2 \right), & \text{if } 0.4 \leq r; \end{cases}$$

where u_0, v_0, p_0 are user-defined real parameters. Notice that a local coordinate system $\tilde{\mathbf{x}} = \mathbf{x} - \mathbf{x}_0$ is employed to define the radial distance $r = (\tilde{x}^2 + \tilde{y}^2)^{0.5}$ from the vortex center $\mathbf{x}_0 = [0.5 \ 0.5]^T$ at the initial simulation time.

Figure 5 shows the initial circumferential velocity u_θ and vorticity $\omega = \nabla \times \mathbf{u}$ fields as function of the radial distance from the vortex center in case of a ‘standing vortex problem’, i.e., $u_0 = v_0 = 0$. Notice the peculiar triangular distribution of the circumferential velocity, from whom the test name originates. Interestingly, the velocity field yields a discontinuous vorticity field: a rigid body rotation core ($r < 0.2$) with constant counter-clockwise vorticity comes in contact with an annular region ($0.2 \leq r < 0.4$) with radially increasing clockwise vorticity followed by an external region ($0.4 \leq r$) with fluid at rest (null vorticity).

The numerical investigation is performed imposing $u_0 = v_0 = 1/3$ (moving vortex), $p_0 = 0$ and setting the viscosity as $\nu = 10^{-5}$. BDF2 implicit time integration [33] with a constant step size $\Delta t = t_F/10^4$ is adopted to advance the solution up to the dimensionless end time $t_F = 3$, resulting in the simulation of one period of the moving vortex. At each time step the nonlinear system is solved using a Newton-Krylov iterative method [21]. We consider $k = 4$ and $k = 7$

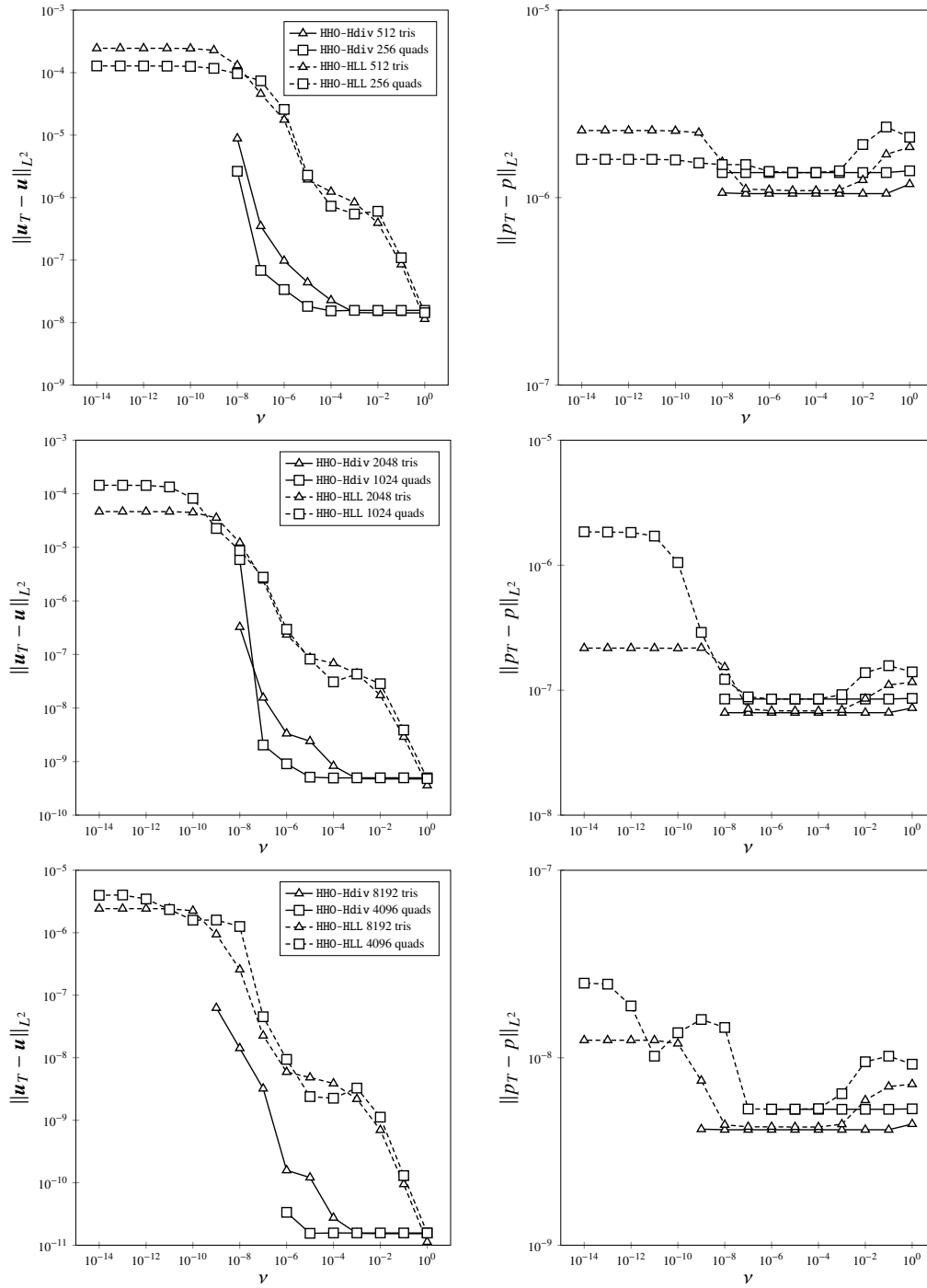


Fig. 3 LLMs pressure gradient. Robustness in the inviscid limit, $k = 3$ HHO-Hdiv (solid lines) and HHO-HLL (dashed lines) formulations. *Left and right*: velocity and pressure error in L^2 -norm, respectively. In each row, from top to bottom, increasingly dense triangular (triangular marks) and quadrilateral (square marks) meshes are considered.

HHO-Hdiv and HHO-HLL formulations on a regular 32×32 quadrilateral elements mesh. The higher polynomial degree is considered as a reference to evaluate the behavior of the lowest order discretization with respect to the evolution of

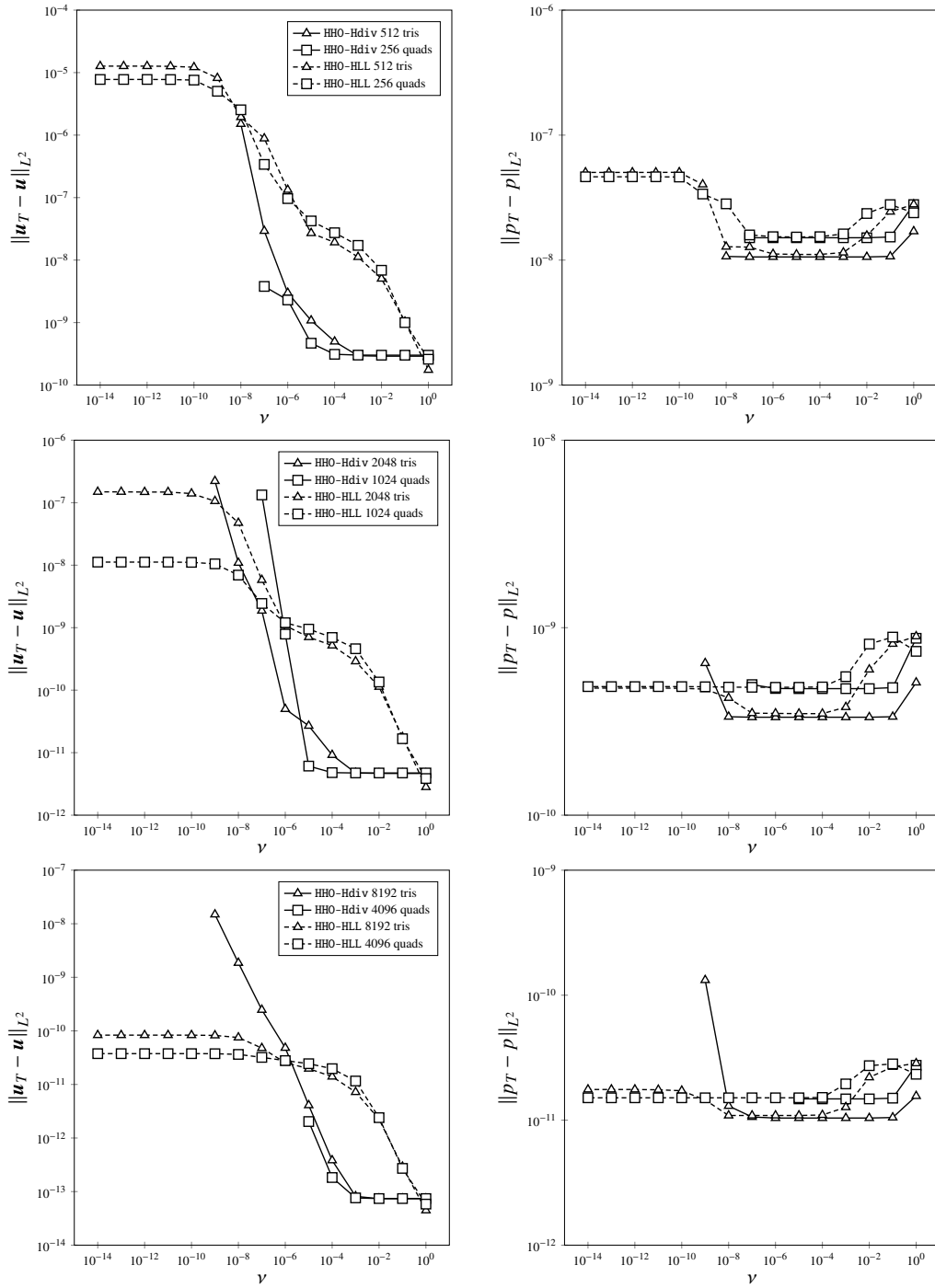


Fig. 4 LLMs pressure gradient. Robustness in the inviscid limit, $k = 4$ HHO-Hdiv (solid lines) and HHO-HLL (dashed lines) formulations. *Left and right*: velocity and pressure error in L^2 -norm, respectively. In each row, from top to bottom, increasingly dense triangular (triangular marks) and quadrilateral (square marks) meshes are considered.

kinetic energy \mathcal{K} and enstrophy \mathcal{E} , defined as follows

$$\mathcal{K} = \frac{1}{2} \int_{\Omega} \mathbf{u} \cdot \mathbf{u}, \quad \mathcal{E} = \frac{1}{2} \int_{\Omega} \boldsymbol{\omega} \cdot \boldsymbol{\omega}.$$

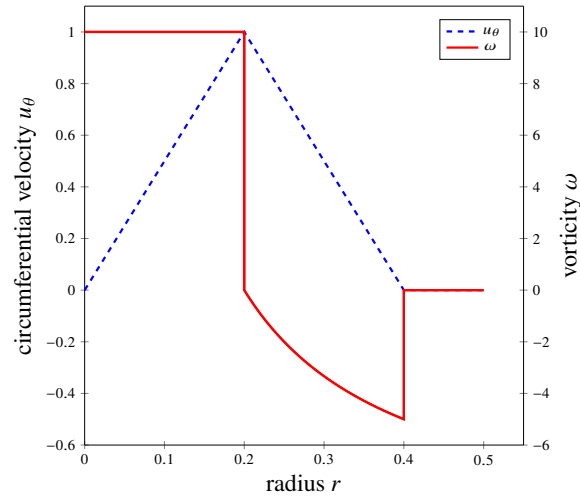


Fig. 5 Gresho-Chan vortex. Radial distribution of the initial circumferential velocity and vorticity fields for the ‘standing vortex problem’ ($u_0 = v_0 = 0$).

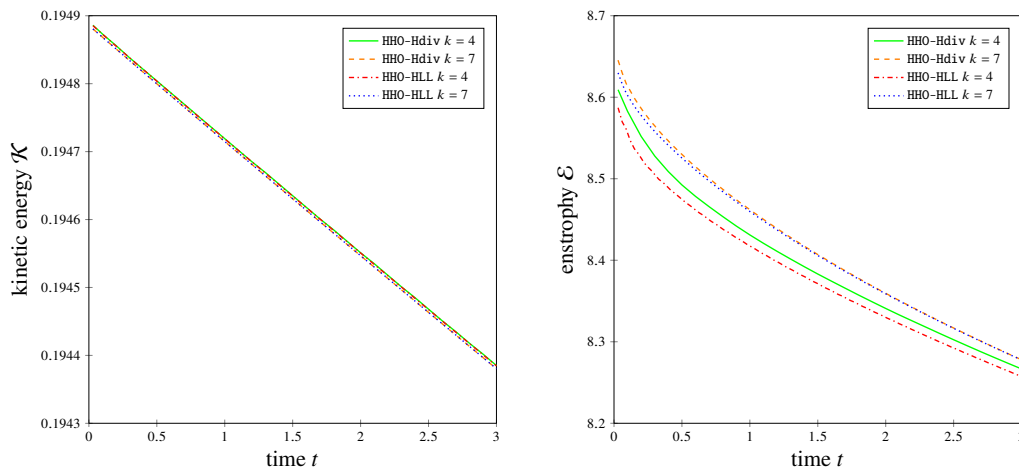


Fig. 6 Gresho-Chan vortex. Kinetic energy \mathcal{K} and enstrophy \mathcal{E} time evolution.

All the simulations performed provide an accurate picture of kinetic energy evolution, see Figure 6. Notice in particular that the kinetic energy decays are superimposed for both schemes and both polynomial degrees. Some differences might be appreciated in terms of enstrophy behavior: while the HHO-HLL and HHO-Hdiv curves are almost superimposed at $k = 7$, at $k = 4$ the HHO-HLL scheme underestimates the enstrophy by a more significant amount.

Figure 7 depicts the vorticity fields at the initial and final simulation times. Because of the discontinuous nature of the initial vorticity field, local over/under-shoots are present at initialization, nonetheless, the final solution looks smoother and the vortex is well resolved. The results suggest that both schemes are capable of satisfactorily preserving vortical structures. Note however that HHO-Hdiv shows some high-frequency oscillations that are absent in the final HHO-Hdiv solution.

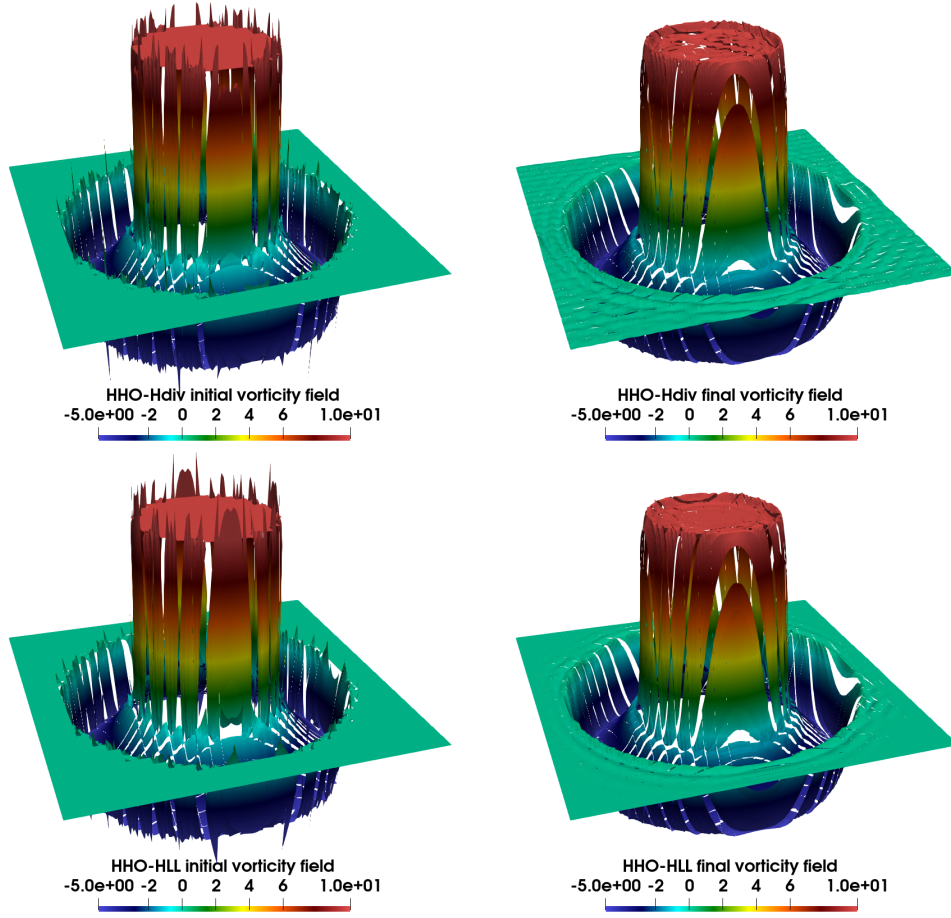


Fig. 7 Gresho-Chan vortex. Vorticity fields (color coded and warped by vorticity magnitude) at $k = 4$. *Left and right*: initial and final simulation times, respectively. *Top and bottom*: HHO-Hdiv and HHO-HLL schemes, respectively.

3.4 Double shear layer

The double shear layer problem devised by Bell *et al.* [13] focuses on inviscid ($\nu = 0$) unsteady flow modelling capabilities. Time integration is performed over a double periodic unit square domain $\Omega = (0, 1) \times (0, 1)$ by means of the BDF2 scheme. The initial horizontal and vertical velocity components are set as

$$u = \begin{cases} \tanh\left(\frac{y - 0.25}{\xi}\right) & y \leq 0.5 \\ \tanh\left(\frac{0.75 - y}{\xi}\right) & y > 0.5 \end{cases}, \quad \text{and} \quad v = \delta \sin(2\pi x),$$

respectively. The pressure field is uniform and the free parameters are set as $\xi = 1/30$ and $\delta = 1/20$.

We consider $k = \{1, 2, 3, 4\}$ HHO-HLL formulations on a h -refined regular quadrilateral elements mesh sequence such that $\text{card}(\mathcal{T}_h) = 64 * 4^i$, $i = 0, 1, 2, 3, 4$. Time integration is carried out in the time interval $(t_0 = 0, t_F = 2]$ utilizing a constant time step $\Delta t = 10^{-3}$. Upon time integration completion, the relative kinetic energy error, defined as

$$\frac{\mathcal{K}(t_0) - \mathcal{K}(t_F)}{\mathcal{K}(t_0)},$$

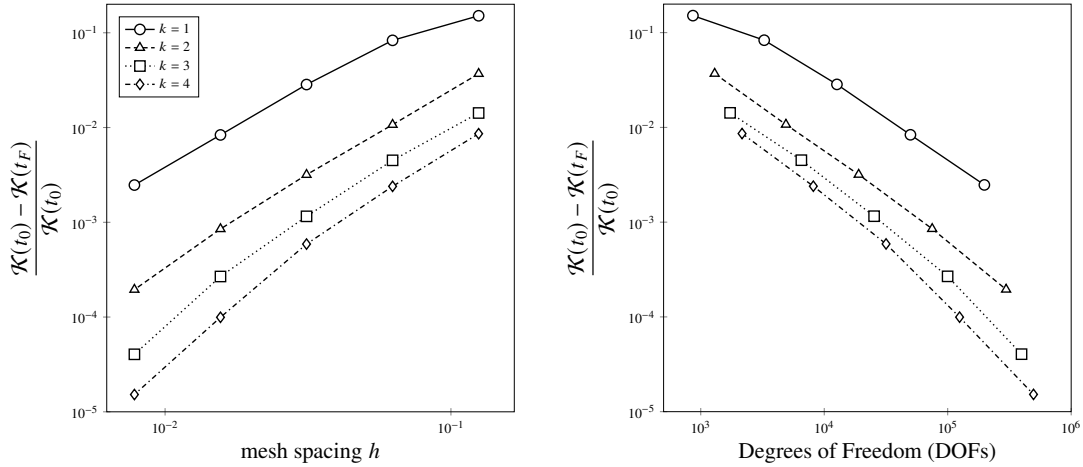


Fig. 8 Double shear layer. HHO–HLL kinetic energy relative error at the final time. *Left and right*: in dependence of the mesh spacing and of the DOFs of the discretized system, respectively.

is a measure of the amount of numerical dissipation introduced by the scheme. Due to its lack of robustness in the inviscid limit, HHO–Hdiv fails to complete the test case, regardless of the polynomial degree and the mesh density, the simulation blows up at early stages. Accordingly only HHO–HLL results are presented hereafter.

In Figure 8 the relative kinetic energy error is plotted against mesh spacing and DOFs. As expected, finer meshes and higher polynomial degrees provide increasingly small numerical dissipation. Moreover, increasing the polynomial degree is always beneficial in terms of error versus DOFs. Considering the finest two grids of the h -refined mesh sequence, the kinetic energy error convergence rates are $\{1.76, 2.13, 2.73, 2.71\}$ for $k = \{1, 2, 3, 4\}$, respectively. Probably, due to the high accuracy required to capture all the flow features, finer meshes and smaller time-steps would be required to reach asymptotic convergence rates. Indeed, as depicted in Figure 9 in case of $k = 4$ HHO–HLL formulations, only the finest mesh allows to satisfactorily represent the tiniest vortical features. This behaviour testifies about the challenges involved in the simulation of the double shear layer.

3.5 Lid-driven cavity flow

We consider the well-known lid-driven cavity flow problem over a unit square domain $\Omega = (0, 1) \times (0, 1)$ at Reynolds $\text{Re} = \frac{1}{\nu} = 10^4$. Dirichlet boundary conditions are imposed on the sliding top wall and the remaining stationary walls. In order to evaluate the robustness of HHO formulations with respect to the mesh distortion we consider a 12768 triangular elements mesh featuring anisotropic and stretched simplexes, see Figure 10. $k = 4$ HHO–HLL and HHO–Hdiv discretizations are applied for seeking steady state solutions starting from fluid at rest.

In Figure 11 the horizontal (u) and vertical (v) velocity components are plotted along vertical ($y = 0.5$) and horizontal ($x = 0.5$) centerlines of the cavity, respectively. The two HHO formulations provide perfectly superimposed velocity profiles and are in very good agreement with reference solutions available from the literature [43, 45].

For the sake of comparison, in Figure 12 we report the warp of the velocity magnitude fields obtained with HHO–Hdiv and HHO–HLL. It is interesting to remark that the most noticeable difference between the two numerical solutions is related to the behavior at the top-left and top-right corners of the cavity, where the velocity is discontinuous and the pressure gradient is steeper. In particular, at the top-left corner, the HHO–Hdiv velocity solution shows a less good agreement with the weakly imposed no-slip boundary condition.

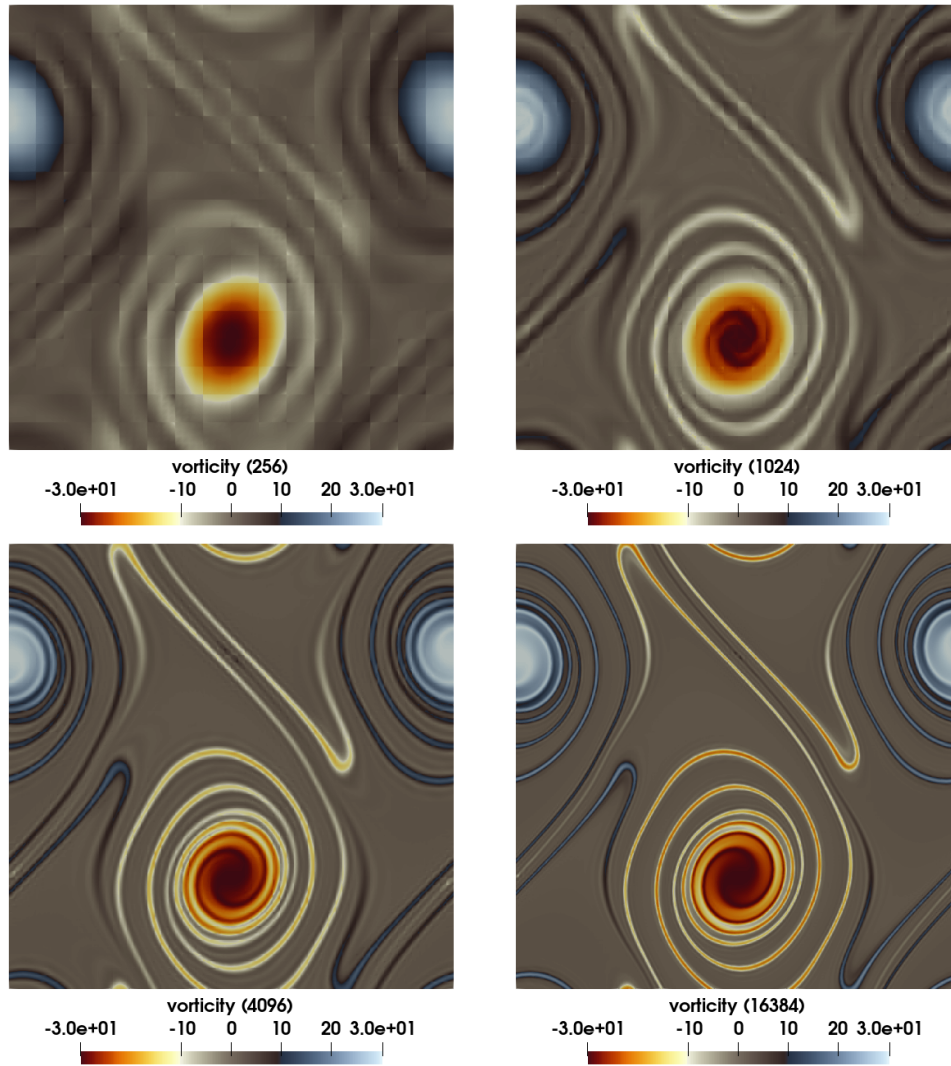


Fig. 9 Double shear layer. Vorticity field at the final time obtained with $k = 4$ HHO-HLL. The mesh cardinality, *i.e.*, 256, 1024, 4096 and 16384 elements, is reported within round brackets.

4 Conclusions

We numerically validated two original Hybrid High-Order formulations designed for seeking approximate solutions of incompressible flow problems. The formulations allow to cope with Dirichlet and Neumann boundary conditions and, in particular, Dirichlet boundary conditions can be imposed weakly. From the accuracy viewpoint both formulations provide increased convergence rates with respect to discontinuous Galerkin discretizations in the diffusion dominated regime. If we consider the polynomial degree leading the size of Jacobian matrix blocks as a reference, HHO h -convergence rates for both velocity and pressure unknowns are one order better than those of dG. In case of HHO-Hdiv the improved convergence rates are maintained up to moderately high Reynolds numbers.

Besides providing numerical convergence rates, pressure-robustness and robustness in the inviscid limit are investigated performing especially conceived test cases. The HHO-HLL scheme, thanks to the introduction of Godunov fluxes based on HHL Riemann Solvers, can be employed for seeking approximate solution of the incompressible Euler equations. The HHO-Hdiv scheme is pressure-robust, kinetic energy preserving and yields mass conservation up to

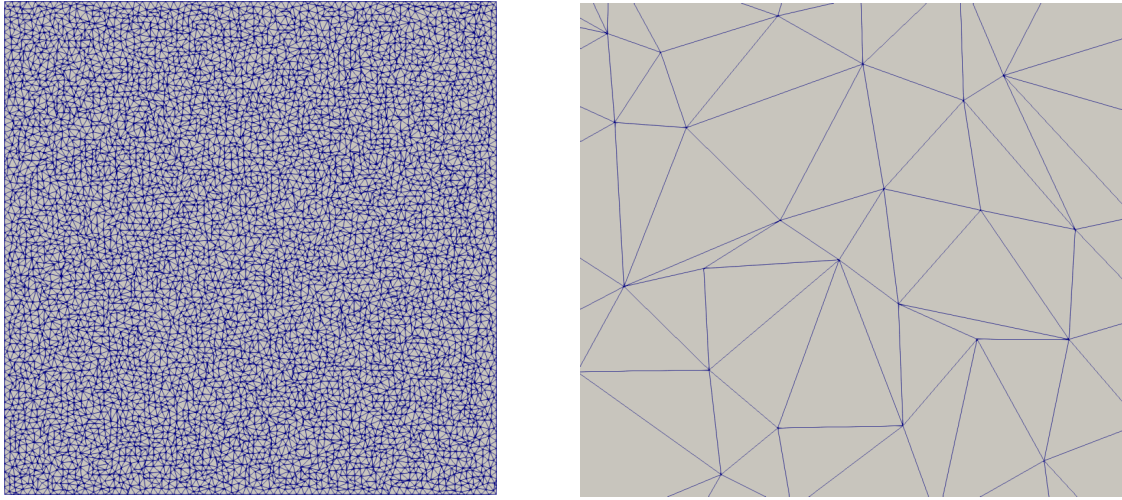


Fig. 10 Lid-driven cavity. Computational mesh. *Left and right*: global and detailed views, respectively.

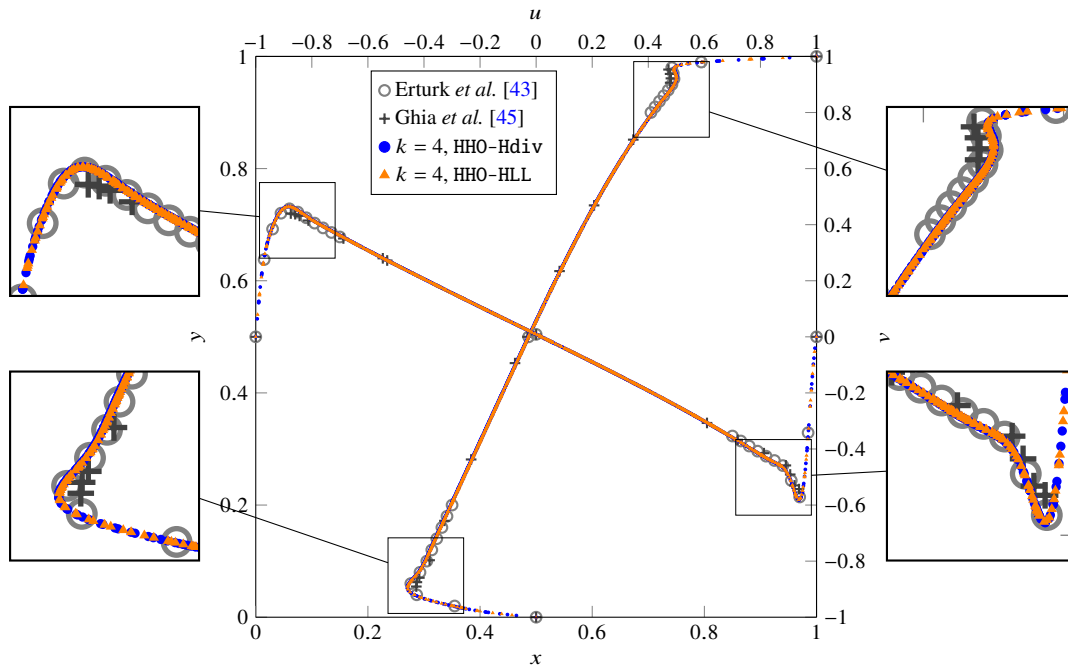


Fig. 11 Lid-driven cavity at $Re = 10k$. Comparison with reference solutions based on horizontal and vertical velocity profiles over vertical and horizontal centerlines, respectively.

machine precision but is not stable in the inviscid limit. Robustness with respect to mesh distortion and grading is demonstrated for both formulations by solving the lid-driven cavity problem at high-Reynolds number over randomly distorted triangular elements meshes.

In conclusion HHO-Hdiv is best suited for low-to-moderate Reynolds number flows, thanks to improved convergence rates and exact mass conservation, while HHO-HLL is able to cope with moderate-to-high Reynolds number flows, hence rivaling dG discretizations based on Godunov fluxes. While in this work we focused on 2D test cases, the formulations are well suited to be applied in 3D. Future works tackling 3D computations are planned but will require further efforts for improving the efficiency of the solution strategy. Indeed, while 2D computations can be effectively carried out

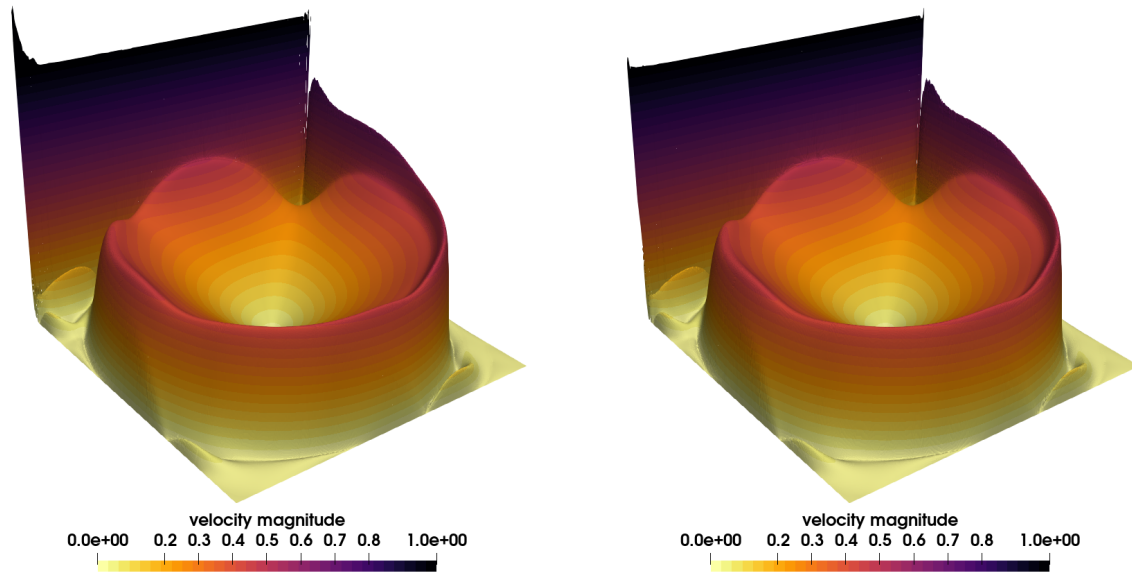


Fig. 12 Lid-driven cavity at $Re = 10k$. Warp of the velocity magnitude field. *Left and right*: HHO-Hdiv and HHO-HLL formulation, respectively.

relying on direct solvers, state-of-the-art preconditioned iterative solvers are required for tackling h -refined 3D mesh sequences.

Declarations

The authors declare that no funds, grants, or other support were received during the preparation of this manuscript. The authors declare that they have no conflict of interest. Data will be made available from the corresponding author on reasonable request.

References

1. Mickaël Abbas, Alexandre Ern, and Nicolas Pignet. Hybrid High-Order methods for finite deformations of hyperelastic materials. *Comput. Mech.*, 62(4):909–928, 2018.
2. J. Aghili, S. Boyaval, and D. A. Di Pietro. Hybridization of mixed high-order methods on general meshes and application to the Stokes equations. *Comput. Meth. Appl. Mat.*, 15(2):111–134, 2015.
3. P. F. Antonietti, A. Cangiani, J. Collis, Z. Dong, E. H. Georgoulis, S. Giani, and P. Houston. Review of discontinuous Galerkin finite element methods for partial differential equations on complicated domains. In *Building bridges: connections and challenges in modern approaches to numerical partial differential equations*, volume 114 of *Lect. Notes Comput. Sci. Eng.*, pages 279–308. Springer, [Cham], 2016.
4. P. F. Antonietti, S. Giani, and P. Houston. hp -version composite discontinuous Galerkin methods for elliptic problems on complicated domains. *SIAM J. Sci. Comput.*, 35(3):A1417–A1439, 2013.
5. Santiago Badia, Jerome Droniou, and Liam Yemm. Conditioning of a Hybrid High-Order scheme on meshes with small faces. arXiv preprint, 2021.
6. F. Bassi, L. Botti, A. Colombo, D. A. Di Pietro, and P. Tesini. On the flexibility of agglomeration based physical space discontinuous Galerkin discretizations. *J. Comput. Phys.*, 231(1):45–65, 2012.
7. F. Bassi, L. Botti, A. Colombo, and S. Rebay. Agglomeration based discontinuous Galerkin discretization of the Euler and Navier-Stokes equations. *Comput. & Fluids*, 61:77–85, 2012.
8. F. Bassi and S. Rebay. A high-order accurate discontinuous finite element method for the numerical solution of the compressible Navier-Stokes equations. *J. Comput. Phys.*, 131(2):267–279, 1997.
9. F. Bassi, S. Rebay, G. Mariotti, S. Pedinotti, and M. Savini. A high-order accurate discontinuous finite element method for inviscid and viscous turbomachinery flows. In R. Decuyper and G. Dibelius, editors, *Proceedings of the 2nd European Conference on Turbomachinery Fluid Dynamics and Thermodynamics*, pages 99–109, 1997.
10. Francesco Bassi, Lorenzo Botti, and Alessandro Colombo. Agglomeration-based physical frame dG discretizations: an attempt to be mesh free. *Math. Models Methods Appl. Sci.*, 24(8):1495–1539, 2014.

11. Francesco Bassi, Andrea Crivellini, Daniele Antonio Di Pietro, and Stefano Rebay. An artificial compressibility flux for the discontinuous Galerkin solution of the incompressible Navier-Stokes equations. *J. Comput. Phys.*, 218(2):794–815, 2006.
12. Francesco Bassi, Francesco Carlo Massa, Lorenzo Alessio Botti, and Alessandro Colombo. Artificial compressibility Godunov fluxes for variable density incompressible flows. *Comput. Fluids*, 169:186–200, 2018.
13. John B. Bell, Phillip Colella, and Harland M. Glaz. A Second-Order Projection Method for the Incompressible Navier–Stokes Equations. *J. Comput. Phys.*, 85:257–283, 1989.
14. L. Botti, D. A. Di Pietro, and J. Droniou. A Hybrid High-Order method for the incompressible Navier–Stokes equations based on Temam’s device. *J. Comput. Phys.*, 376:786–816, 2019.
15. Lorenzo Botti, Michele Botti, and Daniele A. Di Pietro. An abstract analysis framework for monolithic discretisations of poroelasticity with application to Hybrid High-Order methods. *Comput. Math. Appl.*, 91:150–175, 2021. Robust and Reliable Finite Element Methods in Poromechanics.
16. Lorenzo Botti, Michele Botti, and Daniele A. Di Pietro. *A Hybrid High-Order Method for Multiple-Network Poroelasticity*, pages 227–258. Springer International Publishing, Cham, 2021.
17. Lorenzo Botti and Daniele A. Di Pietro. p-Multilevel Preconditioners for HHO Discretizations of the Stokes Equations with Static Condensation. *Commun. Appl. Math. Comput.*, 10 2021.
18. Lorenzo Botti, Daniele A. Di Pietro, and Jérôme Droniou. A Hybrid High-Order discretisation of the Brinkman problem robust in the Darcy and Stokes limits. *Comput. Methods Appl. Mech. Engrg.*, 341:278–310, 2018.
19. M. Botti, D. A. Di Pietro, and P. Sochala. A Hybrid High-Order method for nonlinear elasticity. *SIAM J. Numer. Anal.*, 55(6):2687–2717, 2017.
20. Botti, Michele, Castanon Quiroz, Daniel, Di Pietro, Daniele A., and Harnist, André. A hybrid high-order method for creeping flows of non-Newtonian fluids. *ESAIM: M2AN*, 55(5):2045–2073, 2021.
21. Peter N. Brown and Youcef Saad. Convergence Theory of Nonlinear Newton–Krylov Algorithms. *SIAM J. Optimiz.*, 4(2):297–330, 1994.
22. Andrea Cangiani, Zhaonan Dong, Emmanuil H. Georgoulis, and Paul Houston. *hp-version discontinuous Galerkin methods on polygonal and polyhedral meshes*. SpringerBriefs in Mathematics. Springer, Cham, 2017.
23. Daniel Castanon Quiroz and Daniele A. Di Pietro. A Hybrid High-Order method for the incompressible Navier–Stokes problem robust for large irrotational body forces. *Comput. Math. Appl.*, 79(9):2655–2677, 2020.
24. A. Cesmelioglu, B. Cockburn, and W. Qiu. Analysis of a hybridizable discontinuous Galerkin method for the steady-state incompressible Navier-Stokes equations. *Math. Comput.*, 86(306):1643–1670, 2017.
25. Alexandre Joel Chorin. A numerical method for solving incompressible viscous flow problems. *Journal of Computational Physics*, 2(1):12–26, 1967.
26. B. Cockburn, D. A. Di Pietro, and A. Ern. Bridging the Hybrid High-Order and Hybridizable Discontinuous Galerkin methods. *ESAIM: M2AN*, 50(3):635–650, 2016.
27. B. Cockburn, S. Hou, and C.-W. Shu. The Runge-Kutta local projection discontinuous Galerkin finite element method for conservation laws. IV. The multidimensional case. *Math. Comp.*, 54(190):545–581, 1990.
28. B. Cockburn, G. Kanschat, D. Schötzau, and C. Schwab. Local Discontinuous Galerkin methods for the Stokes system. *SIAM J. Numer. Anal.*, 40(1):319–343 (electronic), 2002.
29. B. Cockburn, S. Y. Lin, and C.-W. Shu. TVB Runge-Kutta local projection discontinuous Galerkin finite element method for conservation laws. III. One-dimensional systems. *J. Comput. Phys.*, 84(1):90–113, 1989.
30. B. Cockburn and C.-W. Shu. TVB Runge-Kutta local projection discontinuous Galerkin finite element method for conservation laws. II. General framework. *Math. Comp.*, 52(186):411–435, 1989.
31. B. Cockburn and C.-W. Shu. The Runge-Kutta local projection P^1 -discontinuous-Galerkin finite element method for scalar conservation laws. *RAIRO Modél. Math. Anal. Numér.*, 25(3):337–361, 1991.
32. B. Cockburn and C.-W. Shu. The Runge-Kutta discontinuous Galerkin method for conservation laws. V. Multidimensional systems. *J. Comput. Phys.*, 141(2):199–224, 1998.
33. Charles Francis Curtiss and Joseph O. Hirschfelder. Integration of Stiff Equations. *PNAS*, 38(3):235–243, 1952.
34. D. A. Di Pietro and J. Droniou. *The Hybrid High-Order method for polytopal meshes*. Number 19 in Modeling, Simulation and Application. Springer International Publishing, 2020.
35. D. A. Di Pietro and A. Ern. Discrete functional analysis tools for discontinuous Galerkin methods with application to the incompressible Navier-Stokes equations. *Math. Comp.*, 79(271):1303–1330, 2010.
36. D. A. Di Pietro and A. Ern. *Mathematical aspects of discontinuous Galerkin methods*, volume 69 of *Mathématiques & Applications (Berlin) [Mathematics & Applications]*. Springer, Heidelberg, 2012.
37. D. A. Di Pietro, A. Ern, and S. Lemaire. An arbitrary-order and compact-stencil discretization of diffusion on general meshes based on local reconstruction operators. *Comput. Meth. Appl. Mat.*, 14(4):461–472, 2014.
38. D. A. Di Pietro, A. Ern, and S. Lemaire. *Building bridges: Connections and challenges in modern approaches to numerical partial differential equations*, chapter A review of Hybrid High-Order methods: formulations, computational aspects, comparison with other methods. Springer, 2016. No 114 in Lecture Notes in Computational Science and Engineering.
39. D. A. Di Pietro and S. Krell. Benchmark session: The 2D Hybrid High-Order method. In C. Cancès and P. Omnes, editors, *Finite Volumes for Complex Applications VIII – Methods and Theoretical Aspects*, pages 91–106, 2017.
40. D. A. Di Pietro and S. Krell. A Hybrid High-Order method for the steady incompressible Navier–Stokes problem. *J. Sci. Comput.*, 74(3):1677–1705, 2018.
41. Michael Dumbser, F. Fambri, I. Furci, M. Mazza, S. Serra-Capizzano, and M. Tavelli. Staggered discontinuous Galerkin methods for the incompressible Navier–Stokes equations: Spectral analysis and computational results. *Numer. Linear Algebr.*, 25(5):2687–2717, 2018.
42. D. T. Elsworth and Euleterio Francisco Toro. Riemann solvers for solving the incompressible Navier–Stokes equations using the artificial compressibility method. Technical Report 9208, College of Aeronautics, Cranfield Institute of Technology, 1992.
43. E. Erturk, T. C. Corke, and C. Gökçöl. Numerical solutions of 2-D steady incompressible driven cavity flow at high Reynolds. *Int. J. Numer. Meth. Fl.*, 48:747–774, 2005.

44. Nicolas R. Gauger, Alexander Linke, and Philipp W. Schroeder. On high-order pressure-robust space discretisations, their advantages for incompressible high Reynolds number generalised Beltrami flows and beyond. *SMAI-JCM*, 5:89–129, 2019.
45. U. Ghia, K. N. Ghia, and C. T. Shin. High-Re solutions for incompressible flow using the Navier–Stokes equations and a multigrid method. *J. Comput. Phys.*, 48:387–411, 1982.
46. Philip M. Gresho and Stevens T. Chan. On the theory of semi-implicit projection methods for viscous incompressible flow and its implementation via a finite element method that also introduces a nearly consistent mass matrix. Part 2: Implementation. *Int. J. Numer. Meth. Fl.*, 11(5):621–659, 1990.
47. C. T. Kelley and David E. Keyes. Convergence analysis of pseudo-transient continuation. *SIAM J. Numer. Anal.*, 35(2):508–523, 1998.
48. Keegan L. A. Kirk and Sander Rhebergen. Analysis of a Pressure-Robust Hybridized Discontinuous Galerkin Method for the Stationary Navier–Stokes Equations. *J. Sci. Comput.*, 81(2):881–897, 11 2019.
49. Leslie I. George Kovasznay. Laminar flow behind a two-dimensional grid. *Math. Proc. Cambridge*, 44(1):58–62, 1948.
50. Robert Jan Labeur and Garth N. Wells. Energy Stable and Momentum Conserving Hybrid Finite Element Method for the Incompressible Navier–Stokes Equations. *SIAM J. Sci. Comput.*, 34(2):A889–A913, 2012.
51. Philip L. Lederer, Alexander Linke, Christian Merdon, and Joachim Schöberl. Divergence-free Reconstruction Operators for Pressure-Robust Stokes Discretizations with Continuous Pressure Finite Elements. *SIAM J. Numer. Anal.*, 55(3):1291–1314, 2017.
52. Juan Manzanero, Gonzalo Rubio, David A. Kopriva, Esteban Ferrer, and Eusebio Valero. An entropy–stable discontinuous Galerkin approximation for the incompressible Navier–Stokes equations with variable density and artificial compressibility. *J. of Comput. Phys.*, 408:109241, 2020.
53. Francesco Carlo Massa, Lukas Ostrowski, Francesco Bassi, and Christian Rohde. An artificial Equation of State based Riemann solver for a discontinuous Galerkin discretization of the incompressible Navier–Stokes equations. *J. Comput. Phys.*, 448:110705, 2022.
54. N.C. Nguyen, J. Peraire, and B. Cockburn. An implicit high-order hybridizable discontinuous Galerkin method for the incompressible Navier–Stokes equations. *J. Comput. Phys.*, 230(4):1147–1170, 2011.
55. Weifeng Qiu and Ke Shi. A superconvergent HDG method for the incompressible Navier–Stokes equations on general polyhedral meshes. *IMA J. Numer. Anal.*, 36(4):1943–1967, 01 2016.
56. Sander Rhebergen and Garth N. Wells. A hybridizable discontinuous Galerkin method for the Navier-Stokes equations with pointwise divergence-free velocity field. *J. Sci. Comput.*, 76(3):1484–1501, 2018.
57. Khosro Shahbazi, Paul F. Fischer, and C. Ross Ethier. A high-order discontinuous Galerkin method for the unsteady incompressible Navier–Stokes equations. *Journal of Computational Physics*, 222(1):391–407, 2007.
58. Maurizio Tavelli and Michael Dumbser. A staggered space–time discontinuous Galerkin method for the three-dimensional incompressible Navier–Stokes equations on unstructured tetrahedral meshes. *J. Comput. Phys.*, 319:294–323, 2016.
59. Maurizio Tavelli and Michael Dumbser. A pressure-based semi-implicit space–time discontinuous Galerkin method on staggered unstructured meshes for the solution of the compressible Navier–Stokes equations at all Mach numbers. *J. Comput. Phys.*, 341:341–376, 2017.
60. Euleterio Francisco Toro. *Riemann Solvers and Numerical Methods for Fluid Dynamics*. Springer-Verlag Berlin Heidelberg, 2009.
61. Jordi Vila-Pérez, Matteo Giacomini, Ruben Sevilla, and Antonio Huerta. Hybridisable Discontinuous Galerkin Formulation of Compressible Flows. *Arch. Comput. Method E.*, 28(2):753–784, 03 2021.